Variability of the Baroclinic and Barotropic Transient Eddy Forcing Associated with Monthly Changes in the Midlatitude Storm Tracks

NGAR-CHEUNG LAU AND MARY JO NATH

Geophysical Fluid Dynamics Laboratory/NOAA, Princeton University, Princeton, New Jersey

(Manuscript received 19 February 1991, in final form 11 June 1991)

ABSTRACT

The heat and vorticity transports by synoptic-scale eddies at various levels between 1000 and 100 mb have been compiled for each winter month of the 1966–84 period using time-filtered daily analyses produced by the U.S. National Meteorological Center. These circulation statistics were used to compute the three-dimensional distributions of the quasigeostrophic geopotential tendency and vertical motion induced by baroclinic and barotropic eddy processes in individual months. The latter fields serve as the basis for describing the synoptic-scale eddy forcing associated with the leading modes of month-to-month variability of the storm tracks over the North Pacific and North Atlantic. These modes are associated with the meridional displacements of the storm-track axes from their climatological positions.

The placement of a storm track at a certain latitude ϕ in a certain month is accompanied by enhanced convergence of eddy heat fluxes poleward of ϕ. In the tropospheric column poleward of the storm track, this baroclinic eddy forcing leads to positive geopotential tendency near the tropopause and negative geopotential tendency near sea level, as well as strong positive temperature tendency and rising motion. In the same month, the convergence of eddy vorticity transport is also enhanced poleward of ϕ. This barotropic forcing results in negative geopotential tendency throughout the troposphere, as well as rising motion and weak negative temperature tendency poleward of ϕ. All of these features appear with reversed polarity in latitudes equatorward of ϕ.

In the upper troposphere, the geopotential tendency induced by vorticity fluxes is stronger than the opposing effects due to heat fluxes, so that the net eddy forcing retains most of the characteristics of the forcing associated with barotropic processes alone, but with considerably reduced amplitudes. Near sea level, the geopotential tendencies induced by heat and vorticity fluxes reinforce each other and are comparable in amplitude. Throughout the troposphere, the patterns of net geopotential tendency exhibit a positive spatial correlation with those of the concurrent monthly averaged height anomaly. The characteristic time scale associated with this constructive eddy forcing in the storm-track region ranges from several days at 1000 mb, to 1–2 months near the tropopause. On the other hand, the eddy-induced temperature tendency is negatively correlated with the local monthly mean temperature anomaly. The dissipative time scale for this thermal forcing in the storm-track region is ~10 days at 850 mb.

The barotropic geopotential tendency and the baroclinic temperature tendency are essentially determined by the convergences of vorticity and heat fluxes, respectively. The eddy-induced secondary circulation plays a minor role in these tendencies.

1. Introduction

In recent diagnostic studies of the extratropical atmospheric circulation, considerable attention has been devoted to the structural and dynamical properties of the wintertime storm tracks over the North Pacific and North Atlantic. These features are located downstream and slightly poleward of the East Asian and North American jet streams. The storm tracks represent the preferred trajectories of weather systems in the middle latitudes and are characterized by enhanced variability with time scales shorter than a week (Blackmon 1976). The behavior of the synoptic disturbances traveling along these storm tracks is similar to that simulated in life-cycle experiments of unstable baroclinic waves (e.g., Simmons and Hoskins 1978). By virtue of the ability of such transient fluctuations to transport heat and momentum (Blackmon et al. 1977), the storm tracks are also active sites of eddy–mean flow interactions. The nature of these interactions between the stationary flow field and the climatological storm tracks has been examined by Lau and Holopainen (1984), Wallace and Lau (1985), Plumb (1986), Holopainen (1990), and others, using circulation statistics averaged over many winters. In view of the considerable variations in both the storm tracks and the ambient flow field on weekly and monthly time scales, some efforts have also been made in the past few years to delineate the impact of synoptic eddies in specific circulation regimes, such as blocking episodes (e.g., Trenberth 1986; Mullen 1987; Holopainen and Fortelius 1987; Dole 1989; Holopainen 1990; and Nakamura and Wallace 1990).

Corresponding author address: Dr. Ngar-Cheung Lau, Geophysical Fluid Dynamics Laboratory, Princeton University, P. O. Box 308, Princeton, NJ 08542.

In a recent article, Lau (1988, hereafter referred to as L) examined the temporal changes in the behavior of the storm tracks during a 19-year period. By using the root-mean-square of time-filtered geopotential height data for a given month as a descriptor of the position and intensity of the storm tracks for that month, several well-defined modes of storm-track variability have been identified in L for each ocean basin. It was demonstrated that these modes are linked to characteristic monthly averaged circulation patterns, many of which bear some resemblance to the recurrent teleconnection patterns documented earlier by Wallace and Gutzler (1981) and others. Hence, the alterations in the geographical location and strength of the storm tracks go hand in hand with systematic changes in the more slowly varying background flow. The evidence presented in L also indicates that the eddy forcing associated with the convergence of vorticity fluxes in individual months tends to reinforce the concurrent monthly mean circulation. Some of the findings in L have since been substantiated by Metz (1989), Anderson and Gyakum (1989), and Rogers (1990).

Due to the lack of a comprehensive set of monthly circulation statistics at the time of the study by L, the diagnosis of eddy forcing reported therein was limited to the *barotropic* effects of vorticity transports at 300 mb only. Neither the vertical dependence of this forcing nor the nature of the *baroclinic* effects of eddy heat transports at various pressure levels were examined in L. Bearing in mind the distinctly baroclinic character of the transient disturbances along the storm tracks, our understanding of the variability of eddy forcing in these sites of synoptic activity would obviously not be complete without a full treatment of the impact of eddy heat fluxes as well. In fact, Lau and Holopainen (1984, hereafter referred to as LH) have already shown that, for the climatological case, the effect of the heat fluxes on the long-term averaged flow in the upper troposphere actually *opposes* that of the vorticity fluxes. It is, hence, important to ascertain the extent to which the constructive forcing in the upper troposphere due to barotropic processes is offset by the dissipative effects of the baroclinic processes on a month-to-month basis. At the 1000-mb level, the climatological results presented in LH indicate that *both* the heat and vorticity fluxes act to reinforce the long-term averaged flow, and that the baroclinic forcing is even stronger than the barotropic effects. The vertical structure of the total eddy forcing would, therefore, be quite different from that obtained by considering vorticity transports or heat transports individually.

The primary object of the present study is to offer a more complete description of the eddy forcing associated with the principal modes of storm-track variability on a monthly time scale. This goal is achieved by taking into consideration the dual effects of vorticity and heat fluxes, and by documenting the three-dimensional distributions of these eddy effects. For this purpose, a voluminous dataset (described in section 2) has been used to compile the requisite variance and covariance statistics for each winter month. The three-dimensional structure of the barotropic and baroclinic components of the eddy forcing for individual months has been obtained by following the procedure outlined in LH, which entails the solution of the quasigeostrophic geopotential tendency and omega equations (see section 3). The leading modes of storm-track variability were identified using the same method as that described in L (see section 4). The eddy forcing accompanying two of the storm-track modes were then illustrated by regression charts of geopotential and temperature tendencies, eddy flux convergences, as well as eddy-induced vertical motion at selected pressure levels (section 5). More general relationships between the eddy forcing and the local monthly averaged circulation anomaly were also examined (section 6).

2. Dataset and analysis procedure

The database for the present study consists of daily analyses (at 1200 UTC) of the analyzed zonal and meridional wind, temperature, and geopotential height for the 18-winter period from 1966 to 1984. Each winter season consists of the 5-month period from November to March. The pressure levels used were 1000, 850, 700, 500, 300, 200, and 100 mb. For the 1000- and 100-mb levels, only the height data were examined. This dataset was produced by the U.S. National Meteorological Center. The data domain extends from 20°N to the North Pole. An elaborate data-checking procedure has been applied to all data grids, and the obviously erroneous fields were expunged from the archives. All missing data grids were then filled by linear interpolation in the time domain. Among the $18 \times 5 = 90$ winter months in this dataset, there were nine months with wide data gaps in some of the variables.[1] The analyses for the latter months were also deleted, so that a total of $90 - 9 = 81$ winter months were used in the present study.

To retain only those disturbances with synoptic time scales, a 21-point bandpass time filter has been applied to the daily data grids. This digital filter was described in Blackmon and Lau (1980) and admits fluctuations with periods ranging from 2.5 to 6 days. For each of the 81 winter months available, the mean quantities were computed using the unfiltered data, whereas second-moment quantities such as the root-mean-square (rms) of geopotential height $(\overline{z'^2})^{1/2}$, and the transient eddy fluxes $\overline{u'v'}$, $\overline{u'u'}$, $\overline{v'v'}$, $\overline{u'T'}$, and $\overline{v'T'}$ were evaluated using the bandpass-filtered data. Here the overbar denotes the average for an individual winter month,

[1] The nine months were February through March 1968; January through February 1970; December 1974–March 1975; and March 1976.

the prime represents the bandpass-filtered quantities, and u, v, and T are the analyzed zonal and meridional wind and temperature, respectively. These variance and covariance statistics provide a detailed description of the eddy characteristics at all tropospheric levels, and for each month in the 81-month sample. As in L, the climatological seasonal cycle has been removed from the statistics for individual months by subtracting from them the long-term means for the corresponding calendar months.

3. Eddy-induced geopotential tendency and vertical motion—formulation and interpretations

In this study, the contributions of transient eddy heat and vorticity fluxes during individual months to the forcing of the mean flow for the same month are illustrated using eddy-induced geopotential tendency and vertical motion. The methodology adopted here is similar to that outlined in LH. The eddy-induced geopotential tendency may be obtained by solving the simplified quasigeostrophic potential vorticity equation

$$\left\{\frac{1}{f}\nabla^2 + f\frac{\partial}{\partial p}\left(\frac{1}{\sigma}\frac{\partial}{\partial p}\right)\right\}\left(\frac{\partial \Phi}{\partial t}\right) = D^H + D^V, \quad (1)$$

where

$$D^H = f\frac{\partial}{\partial p}\left(\frac{\nabla\cdot\overline{\mathbf{V}'\theta'}}{S}\right)$$

and

$$D^V = -(\nabla\cdot\overline{\mathbf{V}'\zeta'})$$

are the eddy forcings due to heat and vorticity fluxes, respectively. Here $\Phi = gz$ is the geopotential, $\sigma = -(\alpha/\theta)(\partial\theta/\partial p)$ is the static stability, θ the potential temperature, α the specific volume, $S = -\partial\theta/\partial p$, ζ the relative vorticity, and all other symbols are used in their conventional meteorological context. Both σ and S are assumed to be functions of pressure only. The latitudinal variation of the Coriolis parameter f is incorporated in the following computations. The convergence of vorticity flux may be expressed in terms of various components of the momentum fluxes, as shown in Holopainen [1978, Eq. (14)]. In order to distinguish the effects of the heat fluxes from those of the vorticity fluxes, Eq. (1) may be solved by inserting the eddy forcing terms D^H and D^V on its rhs separately. We shall henceforth refer to the height tendencies associated with D^H and D^V as Z_t^H and Z_t^V. The tendency associated with the combined effects of D^H and D^V will be denoted as Z_t^{H+V}. The corresponding temperature tendencies may be obtained using the hydrostatic relationships, that is,

$$T_t^H = -\frac{pg}{R}\frac{\partial}{\partial p}Z_t^H,$$

and

$$T_t^V = -\frac{pg}{R}\frac{\partial}{\partial p}Z_t^V,$$

where R is the gas constant. The numerical procedures and the boundary conditions used to solve Eq. (1) are identical to those described in LH (see their section 4), except that the eddy-induced tendencies discussed in that study were computed using circulation statistics averaged over eight winter seasons, whereas the tendencies considered in the present work correspond to eddy forcings for individual winter months. Since no temperature data are available at 1000 and 100 mb, the eddy heat flux convergence has been set to zero in computing both D^H and the upper and lower boundary conditions at these two levels. As was mentioned in LH, the solution thus obtained is identical to that evaluated using the actual heat fluxes at the two boundaries (see also theoretical arguments presented by Bretherton 1966). The vorticity fluxes at 1000 and 100 mb were computed from the daily height data using the geostrophic approximation.

The eddy-induced vertical motion ω may be obtained by solving the quasigeostrophic omega equation (e.g., see Holton 1979, Chapter 6)

$$\left(\frac{1}{f^2}\nabla^2 + \frac{1}{\sigma}\frac{\partial^2}{\partial p^2}\right)\omega = W^H + W^V, \quad (2)$$

where

$$W^H = \frac{1}{f^2}\nabla^2\left(\frac{\nabla\cdot\overline{\mathbf{V}'\theta'}}{S}\right)$$

and

$$W^V = \frac{1}{f\sigma}\frac{\partial}{\partial p}(\nabla\cdot\overline{\mathbf{V}'\zeta'}).$$

We shall use ω^H and ω^V to denote the vertical velocity induced by the eddy forcings associated with the heat fluxes W^H and vorticity fluxes W^V, respectively. Noting that Eq. (2) has a similar form as the tendency equation, ω^H and ω^V for individual winter months may be obtained by following a procedure analogous to that described in section 4 of LH, with the condition that $\omega^H = \omega^V = 0$ at the lateral, as well as the upper and lower boundaries.

To facilitate the physical interpretation of the results to be presented in the following sections, we shall first consider the qualitative nature of the eddy-induced tendencies and vertical motion in the vicinity of the principal storm tracks. By mapping the distributions of temporal variance and covariance circulation statistics, Blackmon et al. (1977), Lau (1979), and others have documented the properties of synoptic-scale transient disturbances during the northern winter. The sites of enhanced eddy activity thus identified are elongated in the zonal direction and span across the North

(a) Heat Fluxes

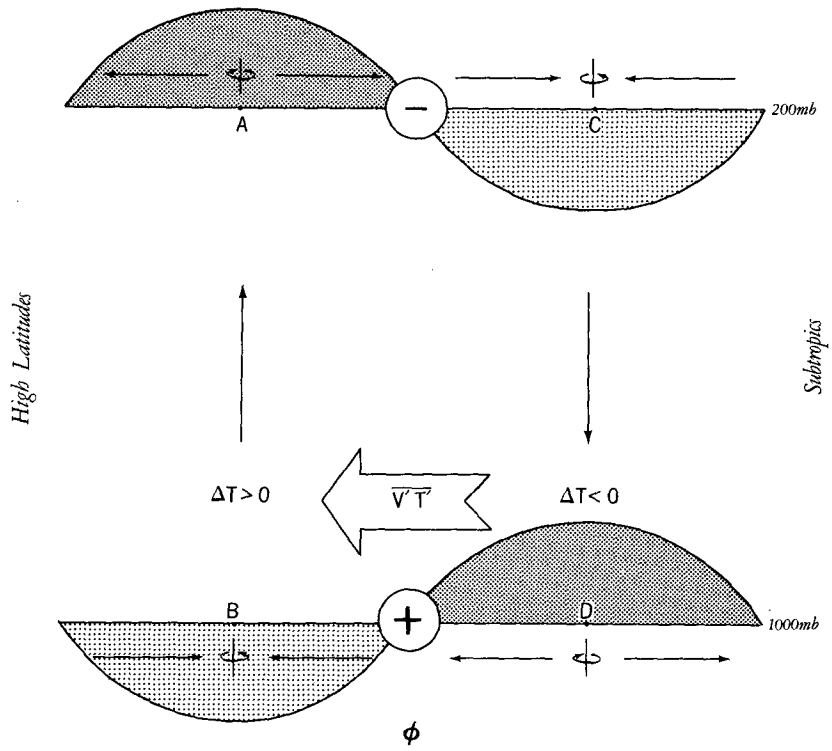

(b) Vorticity Fluxes

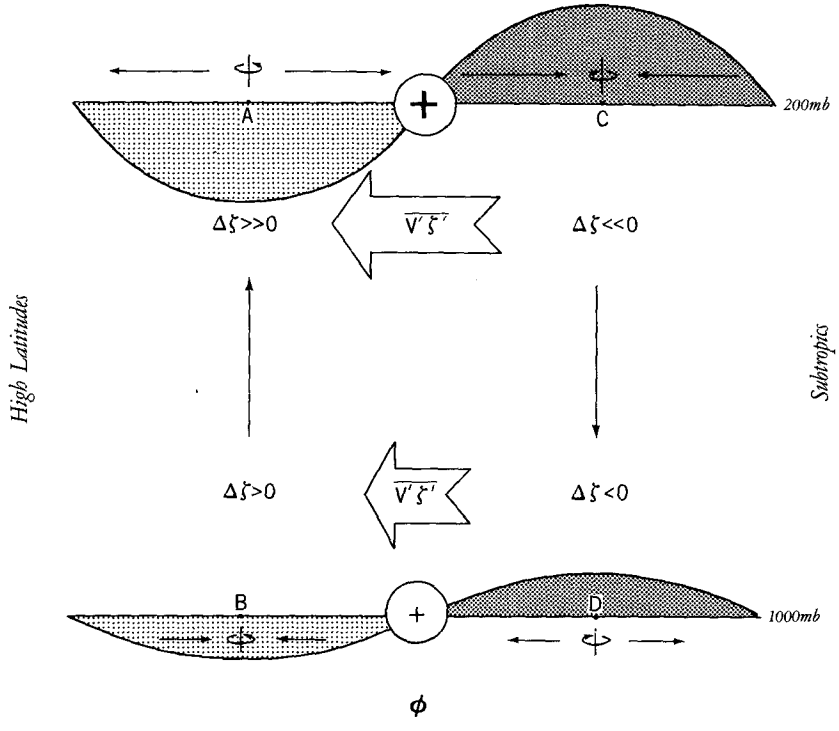

TABLE 1. Polarities of the eddy forcing terms and solutions for the geopotential tendency and omega equations [Eqs. (1) and (2), respectively], as inferred from the spatial configurations of the eddy heat and vorticity flux convergences in relation to a storm-track axis positioned at latitude ϕ. The double pluses and minuses for D^V and Z_t^V at 200 mb indicate that the vorticity forcing in the upper troposphere is stronger than the forcing (of the same sign) near sea level. Polarities are shown only for the region located *poleward* of ϕ. Polarities for the region equatorward of ϕ are opposite of those tabulated here.

	Geopotential tendency equation	
	1000 mb	200 mb
D^H	+	−
D^V	+	++
Z_t^H	−	+
Z_t^V	−	−−
	1000 mb to 200 mb	
T_t^H	+	
T_t^V	−	
	Omega equation 500 mb	
W^H	+	
W^V	+	
ω^H	−	
ω^V	−	

Pacific and North Atlantic (see Fig. 1 of L). The axes of these "storm tracks" typically lie along the 45°–50°N latitudes (hereafter denoted as ϕ). The characteristics of the eddy heat and vorticity transports in the vicinity of these active zones may be summarized as follows:

- The strongest poleward heat flux takes place at ϕ near 850 mb (Blackmon et al. 1977, Fig. 11b), so that divergence of heat transport prevails equatorward of ϕ, and the region farther poleward is characterized by heat flux convergence (Lau 1979, Fig. 20c).
- The most intense poleward vorticity flux occurs at ϕ in the upper troposphere (Lau and Wallace 1979, Fig. 10b), with convergence in the region poleward of ϕ, and divergence on the equatorward flank of the storm-track axis (Lau 1979, Fig. 8).

With these divergence patterns of the heat and vorticity fluxes in mind, the polarities of the forcing terms for Eqs. (1) and (2) in various sectors of the storm-track region may be determined in a straightforward manner. The results are summarized in Table 1. By decomposing both the forcing terms and the solutions of the two equations considered here into Fourier components and following the arguments of Holton (1979, chapter 6), it is seen that the signs of the height tendency and omega motion are opposite to those of their corresponding forcing functions. The polarities of the eddy-induced tendencies and vertical velocity thus obtained are also shown in Table 1. In the region poleward of the storm-track axis, the heat fluxes act to increase the geopotential height in the upper troposphere and decrease the geopotential near the surface. In the same region, the vorticity fluxes force negative height tendencies throughout the troposphere, with the strongest amplitude being located near the tropopause. Both the heat and vorticity fluxes induce rising motion poleward of the storm track and sinking motion farther equatorward. The eddy-induced vertical circulation is hence in the same sense as the zonally averaged "Ferrel cell" in the midlatitudes.

Besides arguing on the basis of the analytic forms of individual forcing functions, the atmospheric response to the eddy flux divergences may also be deduced by applying geostrophic and hydrostatic constraints. Analogous physical reasoning has been used by Holton (1979, chapter 6) in discussing the height tendency and vertical velocity fields for a developing synoptic disturbance. The schematic diagrams shown in Fig. 1 depict the relevant dynamical processes taking place along the meridional plane in the storm-track region. The eddy heat transport across the storm-track axis at ϕ results in the warming of the air column between points A and B, and cooling of the column between C and D (see Fig. 1a). In the region poleward of ϕ, hydrostatic considerations require an increase in the thickness field, which corresponds to a positive geopotential height tendency at A (indicated by dense stippling), and by a negative tendency at B (light stippling). The geostrophic adjustment of the wind field to these pressure changes leads to an anticyclonic tendency at A, and a cyclonic tendency at B (see direction of the spin indicated at these locations). Such alterations in the vorticity field are achieved by divergence at A, and convergence at B. These divergence patterns are, in turn, linked by rising motion above B (see light arrows). Following the nomenclature used by Holton, we shall henceforth refer to the eddy-induced convergence/divergence and vertical motion as the "secondary circulation." Analogous arguments may be invoked to infer the reversed polarities of the tendencies and

FIG. 1. Schematic diagram of the tendencies (sinusoidal curves) and secondary circulations (light arrows) induced by (a) poleward eddy heat fluxes in the lower troposphere, and (b) poleward eddy vorticity fluxes with amplitudes increasing with height, along a meridional plane taken at the longitude of a typical storm track. The midpoint of the x axis in each panel corresponds to ϕ, the latitude of maximum synoptic-scale activity. Positive and negative height tendencies at the 200- and 1000-mb pressure surfaces are depicted by dense and light stippling, respectively. Anticyclonic and cyclonic tendencies are indicated by the directions of the spin symbols (appropriate for the Northern Hemisphere) plotted at representative locations. Eastward (westward) zonal wind tendencies at ϕ are illustrated by plus (minus) signs within open circles.

secondary circulations in the region equatorward of ϕ (i.e., the column between C and D).

The effects of the eddy vorticity fluxes are illustrated in Fig. 1b. The convergence of vorticity transports poleward of the storm track leads to positive vorticity tendencies (and hence negative height tendencies based on geostrophic considerations) at both A and B. However, since the intensity of vorticity fluxes in the troposphere increases with height, the vorticity and height tendencies at A are stronger than those at B. The thickness of the column between A and B therefore decreases. The resulting negative temperature tendency is achieved by the adiabatic cooling associated with rising motion in the middle troposphere. Conversely, the divergence of vorticity fluxes equatorward of ϕ coincides with positive height tendencies and sinking motion. The eddy-induced vertical motions are linked to convergence and divergence patterns in the upper and lower troposphere (see light arrows).

4. Principal modes of storm-track variability and the accompanying monthly mean circulation patterns

The principal modes of storm-track variability on monthly time scales have been identified by applying an empirical orthogonal function (EOF) analysis to the rms fields of bandpass-filtered 500-mb height for 81 individual winter months (see description of data processing procedure in section 2). The Pacific and Atlantic basins have been considered separately. Except for the slight difference in the time span of data coverage, the EOF analysis performed here is identical to that described in section 3a of L. The percentages of explained variance for the first several Pacific and Atlantic eigenvectors obtained in our study are similar to those described in L. The spatial patterns of the two or three leading eigenvectors in each ocean basin for the present dataset (not shown) have a one-to-one correspondence with their counterparts as documented in L. Some reordering of the eigenvectors occurs beyond the second- or third-ranked patterns. For the sake of brevity, we shall henceforth focus our attention on the variability of the eddy forcing associated with the second eigenvector in the Pacific basin (i.e., P2 following the nomenclature used in L), and the first eigenvector in the Atlantic basin (hereafter referred to as A1). These two storm-track modes are selected for in-depth analysis for the following reasons:

- Among all the eigenvectors obtained, P2 and A1 exhibit the strongest relationships with the monthly averaged circulation. In particular, P2 is highly correlated with the Pacific–North American pattern (see Fig. 4b and Table 1 of L) described by Wallace and Gutzler (1981), and A1 is associated with a characteristic monthly mean pattern (see Figs. 5a and 16a, and Table 1 of L), which bears some similarities to the eastern Atlantic pattern (see Wallace and Gutzler) at 500 mb, and the North Atlantic oscillation (see van Loon and Rogers 1978) at sea level.
- Both P2 and A1 are characterized by a dipole-like structure in their respective ocean basins (see Figs. 2b and 3a of L; and Figs. 2a and 3a in the present paper) and portray meridional displacements of zonally elongated storm tracks from month to month. As will be demonstrated in the following sections, the P2 and A1 modes are particularly suited for delineating the spatial relationships between the location of synoptic activity and the corresponding eddy forcing. The similarity between the P2 and A1 modes also facilitates independent checks among the findings obtained separately for the two ocean basins.
- In view of the strong resemblance between the monthly mean height anomalies associated with either of these two storm-track modes and the corresponding height tendency induced by the anomalous vorticity fluxes (see Figs. 11c,d and 12a,b of L), P2 and A1 are probably accompanied by a well-defined set of interactive processes between the synoptic-scale eddies and the ambient flow.

We shall first depict the circulation features pertinent to the P2 and A1 modes by the regression patterns shown in Figs. 2 and 3. The procedure for constructing these patterns follows closely that outlined by Nakamura et al. (1987). For any given meteorological field h and any given storm-track pattern I, the corresponding regression pattern has been obtained by mapping the distribution of linear regression coefficients between the temporal coefficients of the EOF associated with I (i.e., P2 or A1) and the data values of h at individual grid points. This method yields information on both the *spatial pattern* and *amplitude* of the anomalies of h accompanying the storm-track mode I. Since the linear properties of the EOFs are not altered by scaling the temporal coefficients with an arbitrary constant, the following scaling procedure has been applied, so that the amplitudes in the regression charts to be shown here may be interpreted in a straightforward manner:

- A composite pattern of the rms fields of 500-mb bandpass-filtered height corresponding to the eight months (i.e., approximately 10% of the 81-month data sample available) with the largest *positive* EOF coefficients for I was constructed. Similarly, the composite pattern corresponding to the eight months with the largest *negative* coefficients was obtained. The difference between these two composite patterns, which portrays the swing between the opposite extremes of I, was then calculated.
- The EOF coefficients for I were multiplied by a constant scaling factor, so that the amplitudes of the resulting regression pattern of rms of bandpass-filtered 500-mb height are comparable to the amplitudes of the difference composite chart obtained in the previous step. (Since the spatial patterns of the difference composite chart and the regression chart bear a strong spatial resemblance to each other even before any scaling is applied, the scaling factor can easily be determined

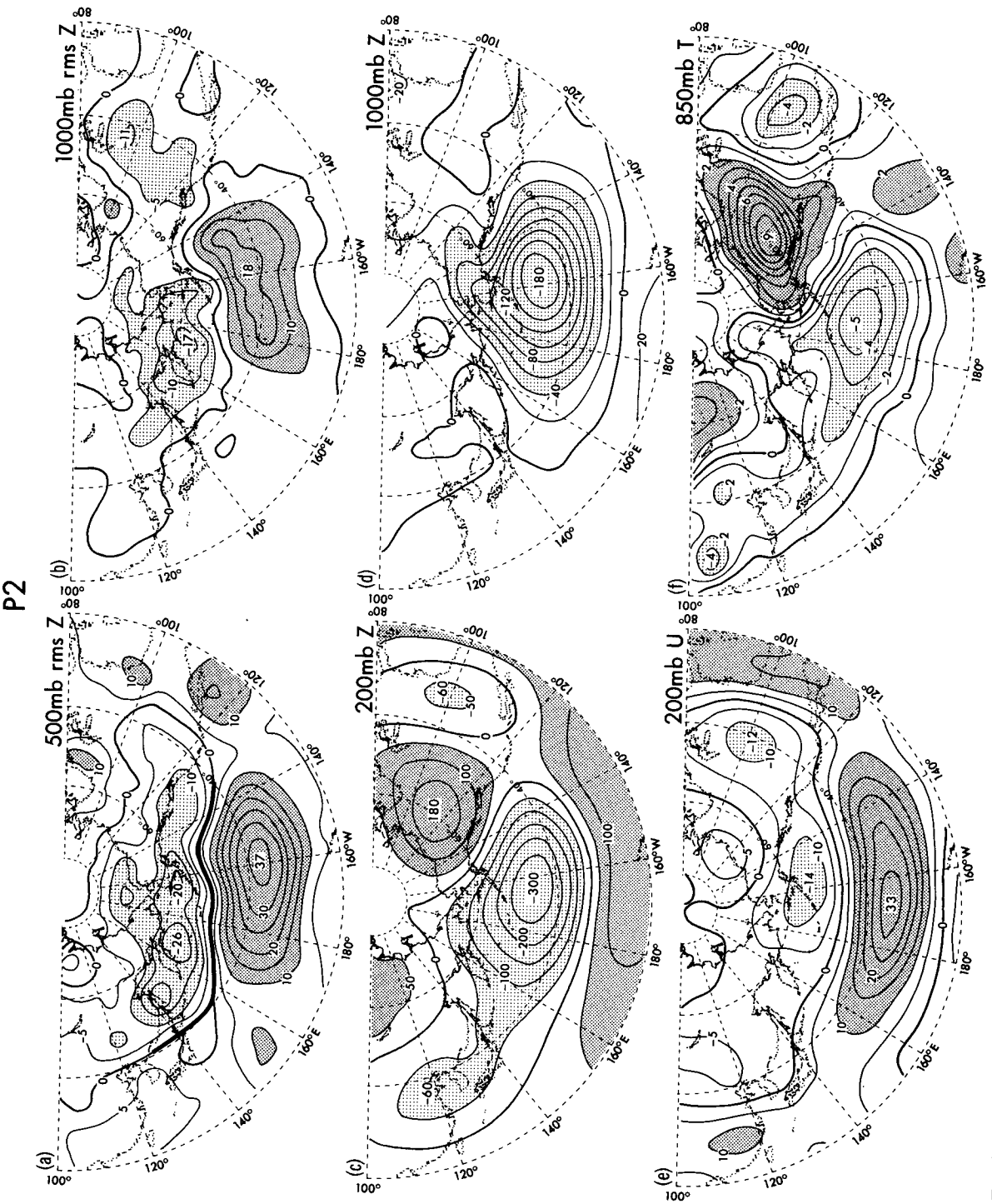

FIG. 2. Distributions of the regression coefficients of the scaled monthly time series of the P2 storm-track mode with gridpoint data of root-mean-square of bandpass-filtered (a) 500-mb height (contour interval: 5 m) and (b) 1000-mb height (contour interval: 5 m); and of monthly means of (c) 200-mb height (contour interval: 50 m), (d) 1000-mb height (contour interval: 20 m), (e) 200-mb zonal wind (contour interval: 5 m s^{-1}), and (f) 850-mb temperature (contour interval: 1°C). The bold line in panel (a) indicates the reference latitude at individual meridians and the longitudinal extent of the averaging domain for constructing the meridional cross sections in Fig. 8. In this and many other figures in this paper, dense and light stippling are used to highlight positive and negative values, respectively.

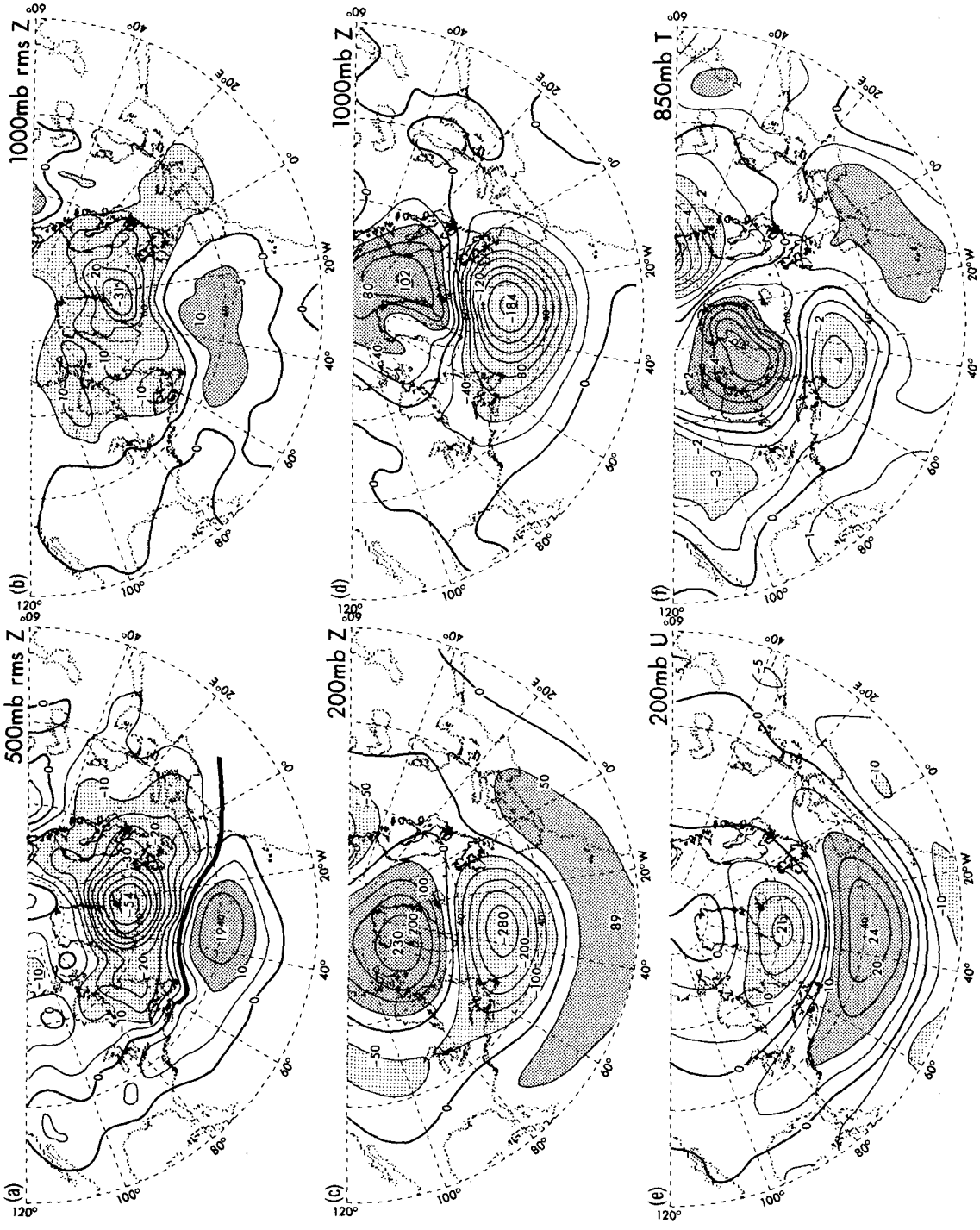

FIG. 3. As in Fig. 2, but for regression coefficients versus time series of the A1 storm-track mode. The bold line in panel (a) indicates the reference latitude at individual meridians and the longitudinal extent of the averaging domain for constructing the meridional cross sections in Fig. 9.

using the representative ratio between the collocated extrema appearing in these two charts.)

The scaled EOF coefficients for P2 and A1 obtained with the aforementioned procedure were used as the reference time series for constructing all regression maps presented in this paper. In view of the scaling method used here, the amplitudes of the regression pattern for any field h and storm-track mode I may be interpreted as being approximately equal to the amplitudes obtained by subtracting the composite of h for 10% of the 81-month data sample with the most negative EOF coefficients for I, from the composite for 10% of the sample with the most positive coefficients. The rationale for presenting our findings using regression patterns in lieu of composite charts is twofold. First, the regression approach provides a convenient framework for weighting the data of h for each month according to the numerical value of the EOF coefficients of I for that month. Second, the information on h for every month in the dataset is utilized in the regression procedure, so that the resulting pattern is representative of the covariability between I and the entire data record for h. On the contrary, most composite procedures would make use of information on h for only those months that exceed a certain threshold for the EOF coefficients of I, and would ascribe equal weights to all data entering into the composites. These distinctions between the regression and composite approaches notwithstanding, detailed comparisons between the composite patterns (not shown) and the corresponding regression charts presented in this study reveal only minor differences. The conclusions to be drawn from the regression charts are therefore not too sensitive to the particular analysis tool employed here. We should also note that the regression statistics to be shown here tend to emphasize linear relationships that are applicable to both the positive and negative phases of a given storm-track mode I. The application of this linear procedure is partially justified by the evidence presented in L (his Fig. 14), who demonstrated that the correspondence between the eddy forcing and the monthly mean circulation does not exhibit any notable dependence on the polarity of I.

Figure 2 shows the regression patterns of the scaled P2 coefficients versus rms of bandpass-filtered heights at (a) 500 mb and (b) 1000 mb, as well as the monthly means of (c) 200-mb height, (d) 1000-mb height, (e) 200-mb analyzed zonal wind, and (f) 850-mb temperature. The corresponding charts associated with the A1 mode are displayed in Fig. 3. To conserve space, the plotting domain is confined to the Pacific basin for Fig. 2 and the Atlantic basin for Fig. 3. The features appearing outside of the plotting domains are generally very weak. Panel (a) in these two figures, which depict the eigenvector patterns associated with the EOF coefficients for P2 and A1, are characterized by a dipolar pattern with the nodal line coinciding with the axis of the climatological storm track in the respective basin (see Fig. 1 of L). Hence, equatorward (poleward) shifts of the storm-track axes prevail in those months with positive (negative) P2 and A1 coefficients. For the P2 pattern (Fig. 2a), the anomaly lying equatorward of the nodal line has a higher amplitude and larger spatial extent than the anomaly located farther poleward. The reverse situation is true for the Al pattern (Fig. 3a). Inspection of Figs. 2b and 3b indicates that meridional migrations of the midtropospheric storm tracks are accompanied by corresponding displacements in the sites of near-surface synoptic activity.

The monthly averaged geopotential height patterns associated with the P2 mode (Figs. 2c,d) have an equivalent barotropic structure over much of the Pacific. These regression maps are very similar to the patterns presented in Figs. 11c and 15b of L on the basis of a composite procedure. The 200-mb chart (Fig. 2c) bears a strong resemblance to the Pacific–North American teleconnection pattern documented by Wallace and Gutzler (1981). The corresponding pattern at the 1000-mb level (Fig. 2d) is dominated by the extremum located over the North Pacific. Comparison among the left panels of Fig. 2 reveals that the two extrema in the rms pattern (Fig. 2a) tend to straddle the North Pacific anomaly in the 200-mb height pattern (Fig. 2c), so that the site of above-normal synoptic-scale variability is collocated with enhanced monthly mean westerlies at 200 mb (Fig. 2e), and vice versa. The regression pattern for monthly mean temperature at 850 mb (Fig. 2f) is highly correlated with the pattern for 200-mb height (Fig. 2c), with above-normal temperatures being accompanied by positive height anomalies, and vice versa.

The relationships between the A1 storm-track mode and the monthly averaged ambient circulation are analogous to those described for the P2 mode. The distinct equivalent barotropic character of the height and temperature fields (Figs. 3c,d, f) and the spatial correspondence between the sites of eddy activity (Fig. 3a) and the monthly mean zonal wind at 200 mb (Fig. 3e) are particularly noteworthy. The 200-mb height anomalies in the Atlantic sector are located in the proximity of the maritime centers of action associated with the eastern Atlantic pattern (Wallace and Gutzler 1981). The 1000-mb height and 850-mb temperature anomalies related to A1 are reminiscent of the circulation changes attending the temperature seesaw between Greenland and northern Europe, as examined by van Loon and Rogers (1978).

5. Variability in the baroclinic and barotropic eddy forcing associated with P2 and A1

We now proceed to examine the monthly changes in the eddy forcing accompanying the storm-track displacements related to the P2 and A1 modes. For any given month in the 81-month data sample, the forcing terms D^H, D^V, W^H, and W^V in the geopotential ten-

dency and omega equations (see section 3) were computed using the bandpass-filtered statistics for eddy fluxes of heat and momentum corresponding to that particular month. The height and temperature tendencies, as well as the eddy-induced vertical motion, were then obtained for each winter month by solving Eqs. (1) and (2) with the method outlined in section 3 and elaborated in L and LH. Solutions associated with the effects of heat fluxes and vorticity fluxes were sought separately. The relationships between the eddy forcing and the storm-track mode I (P2 or A1) were examined by computing regression coefficients of the monthly tendency and omega data grids versus the scaled monthly EOF coefficients for I. As explained in the previous section, the regression maps to be shown here may be interpreted as the composite of the eddy forcing fields weighted according to the magnitude and sign of I in individual months. The amplitudes appearing in these maps provide for an approximate measure of the difference in eddy forcing between the two groups of months with I in the top and bottom tenth percentiles, respectively.

a. Height tendencies

In Fig. 4 the regression patterns are shown for the P2 mode of the height tendencies induced by eddy heat fluxes Z_t^H, eddy vorticity fluxes Z_t^V, and the total effects of heat and vorticity fluxes Z_t^{H+V}, at the 200- (left panels) and 1000-mb (right panels) levels. The two pressure surfaces have been chosen for display here because the regression statistics attain extremum values at these levels. The corresponding patterns associated with the A1 mode are presented in Fig. 5. While interpreting the patterns in Figs. 4 and 5, it is helpful to bear in mind that the anomalous eddy forcing depicted here is due to an equatorward displacement of the storm-track axis in the respective ocean basin (see Figs. 2a and 3a), so that the synoptic activity is enhanced along the 35°–40°N zone (hereafter referred to as ϕ^S, where the superscript S denotes strong eddy activity) and suppressed near 55°–65°N (hereafter referred to as ϕ^W, where the superscript W denotes weak eddy activity). It is seen that the spatial relationships between the eddy-induced height tendencies and the sites of anomalous eddy activity are consistent with those anticipated in section 3 (see Table 1 and Fig. 1) on the basis of qualitative dynamical considerations. Specifically, the patterns in Figs. 4a–d and 5a–d indicate that the region poleward of ϕ^S and equatorward of ϕ^W is characterized by positive anomalous Z_t^H at 200 mb, negative Z_t^H at 1000 mb, and negative Z_t^V throughout the troposphere. The polarities of these tendencies are reversed in the region equatorward of ϕ^S. The anomalies of Z_t^H in the lower and upper troposphere have similar amplitudes but opposite signs. The anomalies for Z_t^V retain the same polarity at 200 and 1000 mb, with the amplitudes at the upper level being higher than those at the lower level by 30%–50%. At the tropopause level, the pattern of Z_t^H exhibits a negative spatial correlation with that of Z_t^V, with the effects of the vorticity fluxes being stronger than those of the heat fluxes by 50%–80%. As a result, the pattern of the total eddy forcing Z_t^{H+V} at 200 mb (Figs. 4e and 5e) is still similar to, but considerably weaker than, that of the forcing due to vorticity fluxes alone. Near the lower boundary, the patterns for Z_t^H and Z_t^V resemble each other both in amplitude and in polarity, so that the total forcing (Figs. 4f and 5f) is approximately twice that of the individual effects due to heat or vorticity fluxes. The spatial configuration of the height tendencies shown in Figs. 4 and 5 in relation to the anomalous storm tracks agrees well with that of the long-term averaged tendencies in relation to the climatological storm tracks, as shown in LH (see their Fig. 3). The dominance of Z_t^V over Z_t^H in the upper troposphere is more evident in the climatological case (compare Figs. 3a and 3c in LH) than is indicated in Figs. 4 and 5 of this paper. This apparent distinction between the two studies is partially due to the different pressure levels used for mapping the height tendencies (i.e., 300 mb in LH versus 200 mb in this paper). As will be demonstrated later in this section (see Figs. 8a and 9a), the upper-level extrema in Z_t^H are located at 200 mb. We hence expect a stronger degree of cancellation between the long-term averaged Z_t^H and Z_t^V at the latter level.

The spatial relationship between the eddy forcing and the contemporaneous mean flow pattern may be appreciated by comparing the height tendency patterns in Figs. 4 and 5 with the regression charts of anomalous monthly averaged height fields for the corresponding storm-track modes (Figs. 2c,d and 3c,d). At 200 mb, the anomalous monthly mean height patterns are positively correlated with Z_t^V, but negatively with Z_t^H. Hence, the eddy vorticity fluxes tend to reinforce the local monthly mean height anomaly in the upper troposphere, whereas the eddy heat fluxes act to oppose the monthly mean height changes. The residual forcing Z_t^{H+V} at the tropopause level still retains a positive spatial correlation with the monthly averaged height field. At the 1000-mb level, the anomalous monthly mean height patterns exhibit the same polarity as that of the patterns for both Z_t^V and Z_t^H. Hence, the barotropic and baroclinic processes act in concert to maintain the monthly mean height anomalies near sea level. Comparison between the 200- and 1000-mb patterns of Z_t^{H+V} clearly indicates that the combined eddy forcing is much stronger near the lower boundary than in the upper troposphere.

b. Temperature tendencies

The regression charts of the 850-mb temperature tendencies due to heat and vorticity fluxes are shown in Fig. 6 for the P2 pattern (left panels) and the A1 pattern (right panels). As can be expected from the

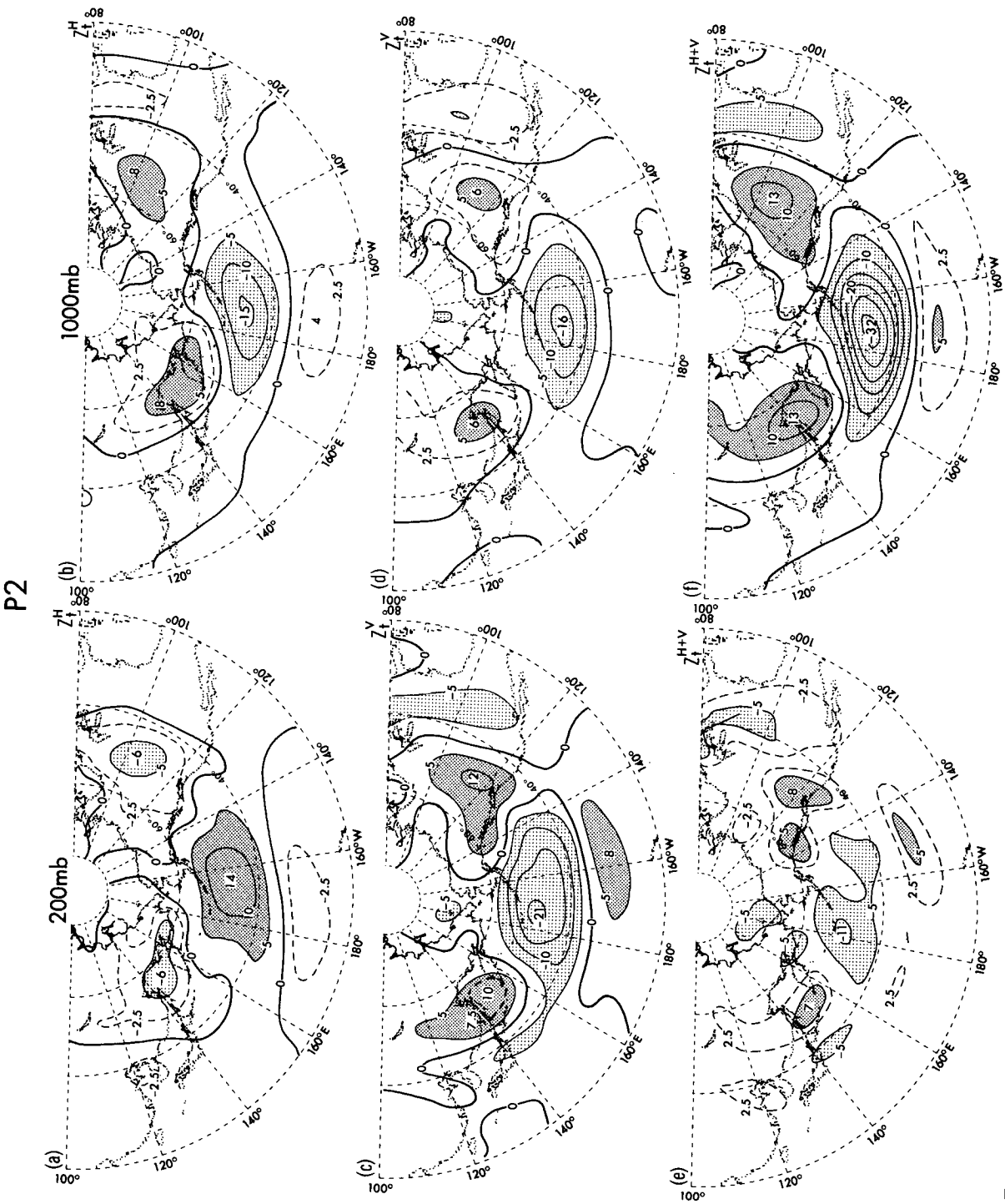

FIG. 4. Distributions of the regression coefficients of the scaled monthly coefficients of the P2 storm-track mode with gridpoint data of height tendency induced by eddy heat fluxes [panels (a) and (b)], eddy vorticity fluxes [panels (c) and (d)], and the sum of eddy heat and vorticity fluxes [panels (e) and (f)]. Results for the 200- and 1000-mb levels are displayed in the left-hand and right-hand panels, respectively. Interval between solid contours: 5×10^{-5} m s^{-1}. The zero contour is omitted in panel (e).

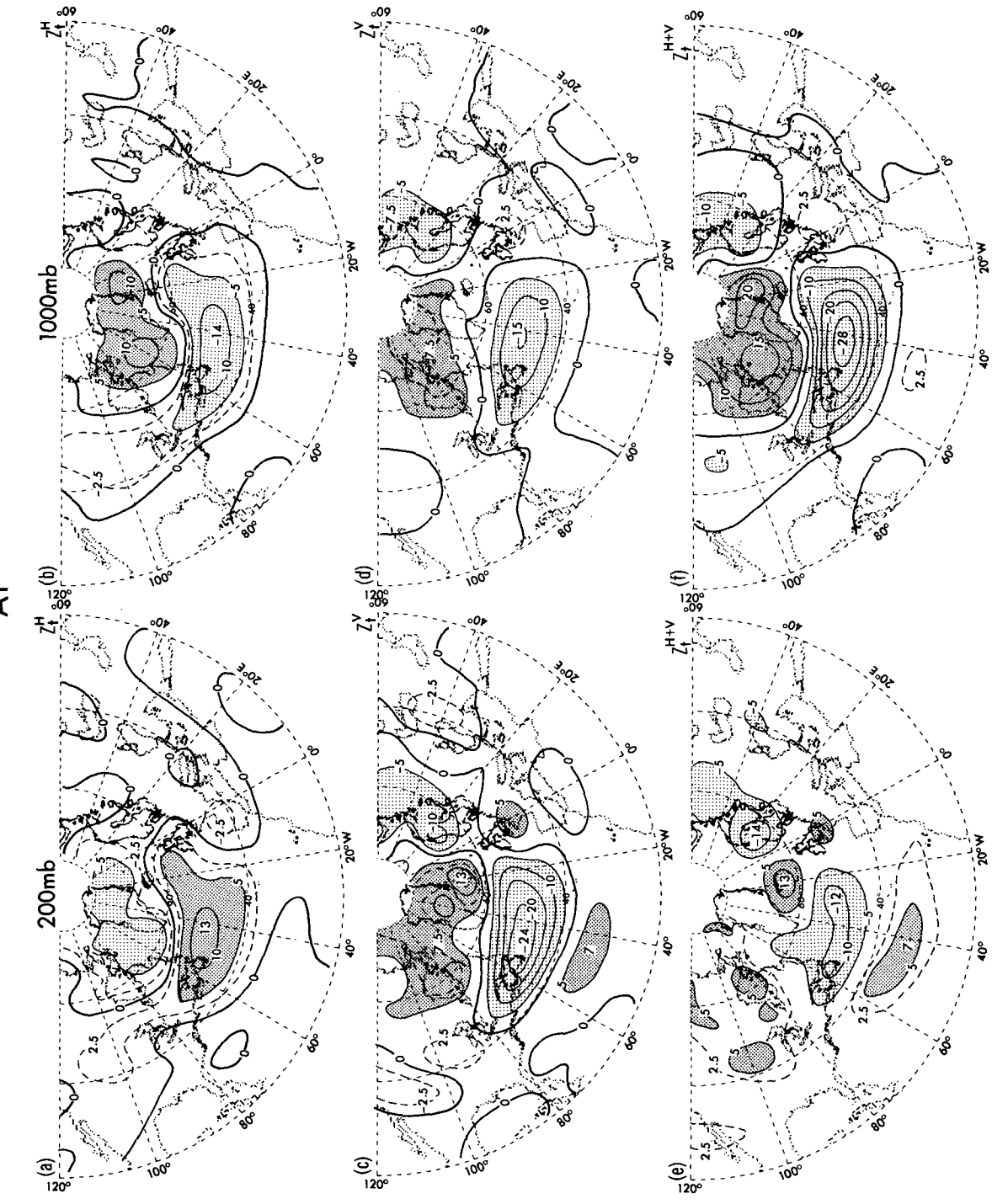

FIG. 5. As in Fig. 4, but for regression coefficients versus time series of the A1 storm-track mode.

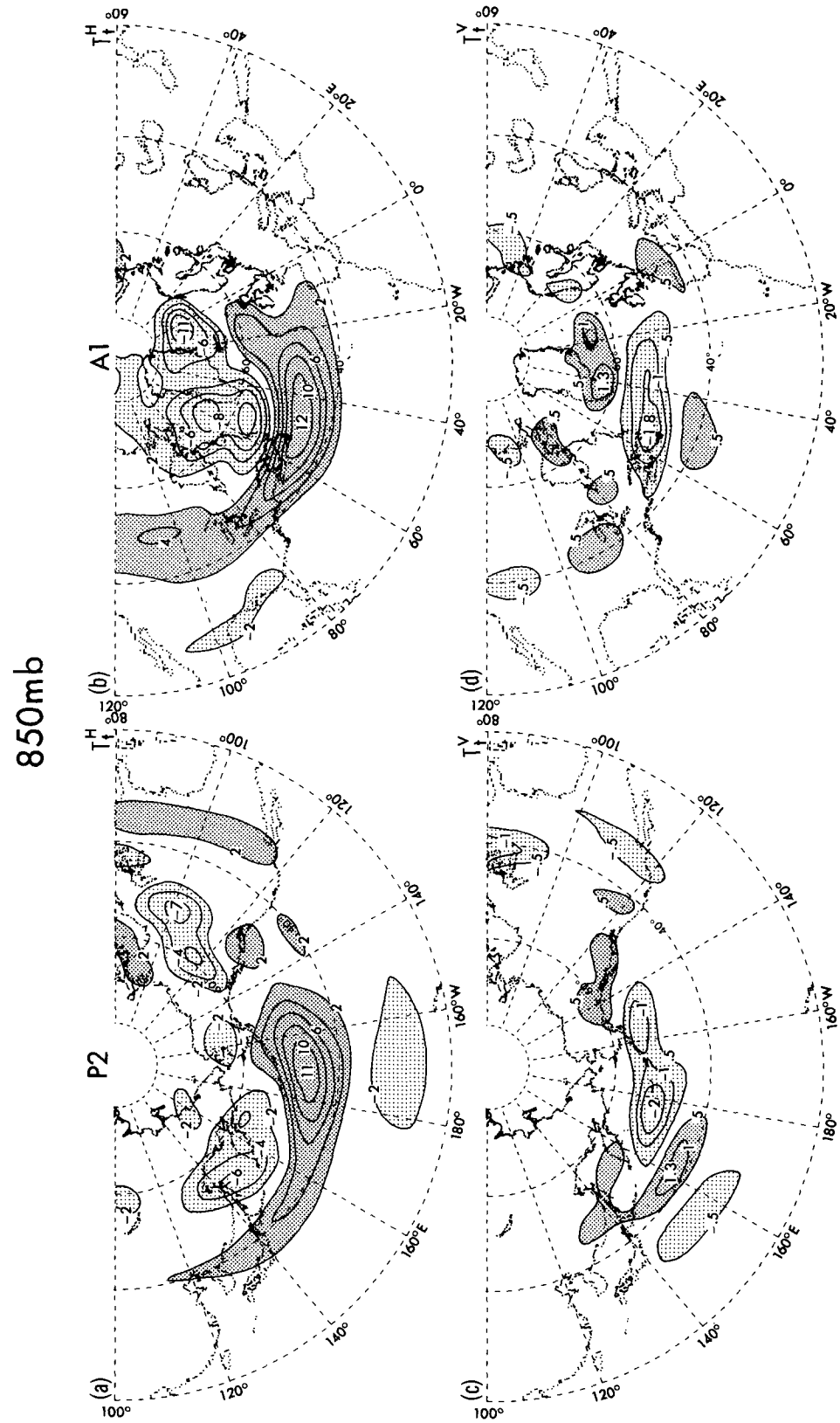

FIG. 6. Distributions of the regression coefficients of the scaled monthly coefficients of the P2 (left panels) and A1 (right panels) storm-track modes with gridpoint data of 850-mb temperature tendency induced by eddy heat fluxes [panels (a) and (b), contour interval: 2×10^{-6} °C s^{-1}], and eddy vorticity fluxes [panels (c) and (d), contour interval: 5×10^{-7} °C s^{-1}]. The zero contour is omitted.

hydrostatic relationship, these patterns are closely related to those for the height tendencies (Figs. 4 and 5). The temperature tendencies associated with heat fluxes are typically stronger than those associated with vorticity fluxes by a factor of 5–10. The pattern for T_t^H is characterized by anomalous warming between ϕ^S and ϕ^W, and cooling equatorward of ϕ^S and poleward of ϕ^W. The relationship between T_t^H and the local monthly mean temperature fluctuations is revealed by comparing the patterns in Figs. 6a,b with the corresponding monthly averaged temperature regression fields (Figs. 2f and 3f). It is seen that warm monthly mean temperature anomalies are coincident with negative temperature tendencies, and vice versa. Hence, the eddy heat fluxes act to destroy the concurrent monthly mean temperature anomalies. The much weaker T_t^V exhibits a negative spatial correlation with T_t^H, with negative tendencies in the zone between ϕ^S and ϕ^W, and positive tendencies farther poleward and equatorward. All of these features are again in accord with the spatial configuration of temperature tendencies deduced qualitatively on the basis of geostrophic and hydrostatic considerations (see section 3).

c. *Vertical motion*

The regression patterns of eddy-induced pressure velocity at 500 mb due to heat fluxes ω^H and vorticity fluxes ω^V are displayed in Fig. 7 for the P2 (left panels) and A1 (right panels) modes. The principal features in this figure agree well with the conceptual framework of the secondary circulation as outlined in section 3 (see Table 1 and Fig. 1). The vertical motions induced by the heat and vorticity fluxes at a given location generally have the same polarity. Anomalous rising motion prevails poleward of the latitude of enhanced eddy activity ϕ^S, whereas anomalous sinking motion is discernible in regions equatorward of ϕ^S. Conversely, subsidence (ascent) is found poleward (equatorward) of the zone of reduced eddy activity ϕ^W. For the P2 mode, the amplitudes of ω^H are typically higher than those of ω^V by 60%–100% over the central Pacific, whereas ω^H and ω^V associated with A1 have comparable intensities.

d. *Vertical structure of eddy-induced tendencies and pressure velocity*

The characteristic vertical dependence of the eddy forcings described in the previous subsections may be delineated using meridional cross sections taken at the longitudinal sectors where the storm-track displacements occur. In order to obtain representative vertical structures, we have performed averages of the eddy-induced tendencies and vertical motion across the length of the storm-track regions. Since the axes of the extrema appearing in the modal patterns of P2 and A1 (Figs. 2a and 3a) are not oriented exactly in the east–west direction, the averaging procedure has been conducted with respect to a reference latitude, which mostly corresponds to the nodal lines in the regression charts for the rms of filtered 500-mb height (see bold lines in Figs. 2a and 3a). The longitudinal extents of these bold lines define the widths of the respective averaging domains. The grid points lying along a given meridian within the domain were classified according to their position (in degrees of latitude, and whether poleward or equatorward) relative to the reference latitude for the same meridian. In order to emphasize the features in regions with the most significant redistribution of synoptic activity, the regression data along a given meridian have been weighted by the sum of the absolute values of the two extrema appearing in Figs. 2a or 3a for the same meridian. (Given the dipole-like structure of Figs. 2a and 3a, there are always two extrema in the rms of 500-mb height along each meridian in the averaging domain, with the maximum and minimum lying equatorward and poleward of the relative latitude, respectively.) The averaging process was then conducted across the domain by grouping the weighted regression data values at all grid points with the same meridional displacement from the local reference latitude. The resulting distributions of various eddy-induced tendencies and vertical motion with respect to pressure and relative latitude are displayed in Fig. 8 for the P2 mode and in Fig. 9 for the A1 mode. The reference latitude is placed at the midpoint of the x axis of the individual panels, with negative and positive relative latitudes indicating equatorward and poleward displacements from the reference latitude, respectively. In Figs. 2a and 3a, the latitude of enhanced eddy activity ϕ^S corresponds to $-10° \sim -15°$ along the x axis presented in Figs. 8 and 9, whereas the latitude of below-normal eddy activity ϕ^W corresponds to approximately $+10° \sim +15°$.

The patterns for the regression coefficients of height tendencies (top panels of Figs. 8 and 9) clearly illustrate the opposite polarities of Z_t^H at the 200- and 1000-mb levels, and the equivalent barotropic structure of Z_t^V, with maximum amplitudes being located at 200 mb. These distributions also highlight the opposing height tendencies due to heat and vorticity fluxes in the upper troposphere, and cooperating tendencies in the lower troposphere. The corresponding pattern for the combined effects of heat and vorticity fluxes Z_t^{H+V} (not shown) still bear some qualitative resemblance to Z_t^V, with the exception that the largest amplitudes in the combined pattern are located at 1000 mb. The zonal wind tendencies U_t^H and U_t^V (not shown) may be inferred from the corresponding height tendencies using the geostrophic relationship. It is seen that U_t^H at ϕ^S is characterized by deceleration of the westerly wind in the upper troposphere, acceleration in the lower troposphere, and hence reduction in the thermal wind, whereas enhancement of the thermal wind occurs at ϕ^W. On the other hand, U_t^V is positive throughout the troposphere at ϕ^S, and is negative at ϕ^W. The above

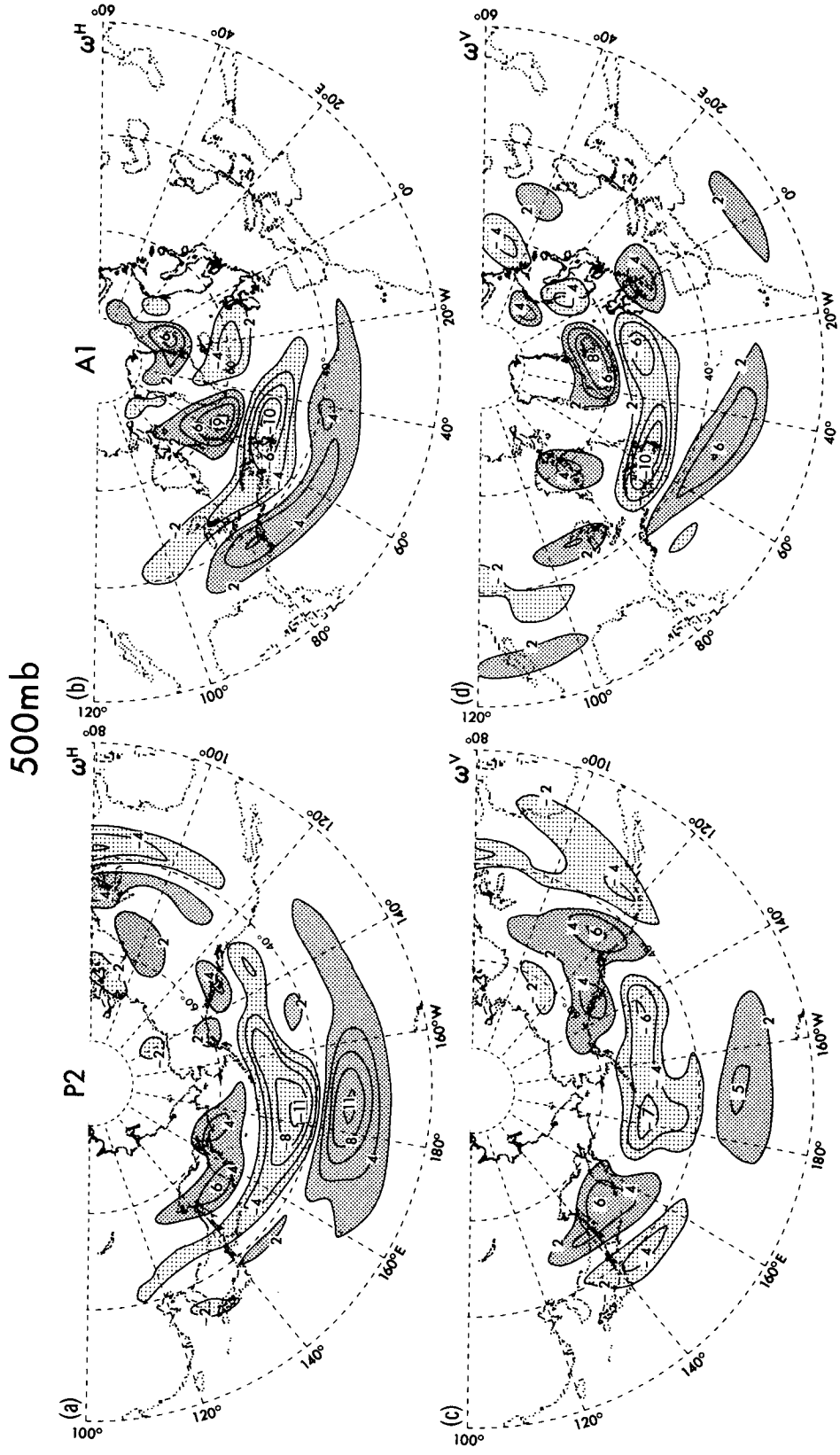

FIG. 7. Distributions of the regression coefficients of the scaled monthly coefficients of the P2 (left panels) and A1 (right panels) storm-track modes with gridpoint data of 500-mb pressure velocity induced by eddy heat fluxes [panels (a) and (b)] and eddy vorticity fluxes [panels (c) and (d)]. Contour interval 2×10^{-5} mb s^{-1}. The zero contour is omitted.

characteristics of U_t^H and U_t^V are in accord with those portrayed in Fig. 1 (see plus and minus signs within open circles).

The cross sections for temperature tendencies (middle panels of Figs. 8 and 9) indicate that the heat fluxes contribute to warming of the tropospheric column within the zone between ϕ^S and ϕ^W, with maximum effects occurring at 850 mb, whereas vorticity fluxes lead to cooling in the same region. Negative T_t^H values prevail equatorward of ϕ^S and poleward of ϕ^W. The dominance of the heat transports in forging temperature changes is also apparent from these panels. The polarities of the considerably weaker T_t^V features are generally opposite to those of T_t^H.

The distributions of the vertical motion induced by both heat and vorticity fluxes (bottom panels of Figs. 8 and 9) are characterized by ascent between ϕ^S and ϕ^W, and by subsidence equatorward of ϕ^S and poleward of ϕ^W. The strongest vertical velocities occur at about 500 mb.

e. *Relative contributions of eddy flux convergences and secondary circulations to the height and temperature tendencies*

In order to delineate the respective roles of flux convergences and secondary circulations (see definition in section 3) in the eddy forcing, it is useful to consider the following simplified vorticity and temperature equations:

$$\zeta_t^{H+V} = \zeta_t^H + \zeta_t^V$$

$$= -(\nabla \cdot \overline{\mathbf{V}'\zeta'}) + f\frac{\partial}{\partial p}\omega^H + f\frac{\partial}{\partial p}\omega^V \quad (3)$$

$$\theta_t^{H+V} = \theta_t^H + \theta_t^V = -(\nabla \cdot \overline{\mathbf{V}'\theta'}) + \omega^H S + \omega^V S \quad (4)$$

where ζ_t and θ_t are the eddy-induced vorticity and potential temperature tendencies, respectively, the superscripts H and V refer to the contributions from the heat and vorticity fluxes, and S is again defined as $-\partial\theta/\partial p$. The eddy heat fluxes contribute to vorticity (and hence geopotential height) tendencies in Eq. (3) solely through stretching effects of the vertical motion induced by the same fluxes [i.e., $\zeta_t^H = f(\partial\omega^H/\partial p)$]. Analogously, the eddy vorticity fluxes lead to temperature changes in Eq. (4) only through adiabatic processes associated with the corresponding secondary circulation (i.e., $\theta_t^V = \omega^V S$). These inferences are clearly demonstrated by the results presented earlier in this section. For instance, comparison of the relevant panels of Figs. 4, 5, 8, and 9 indicates that rising motion induced by heat fluxes is accompanied by positive Z_t^H (and hence negative vorticity tendencies) at 200 mb, where $\partial\omega^H/\partial p < 0$, and by negative Z_t^H at 1000 mb, where $\partial\omega^H/\partial p > 0$. The polarities of Z_t^H are opposite

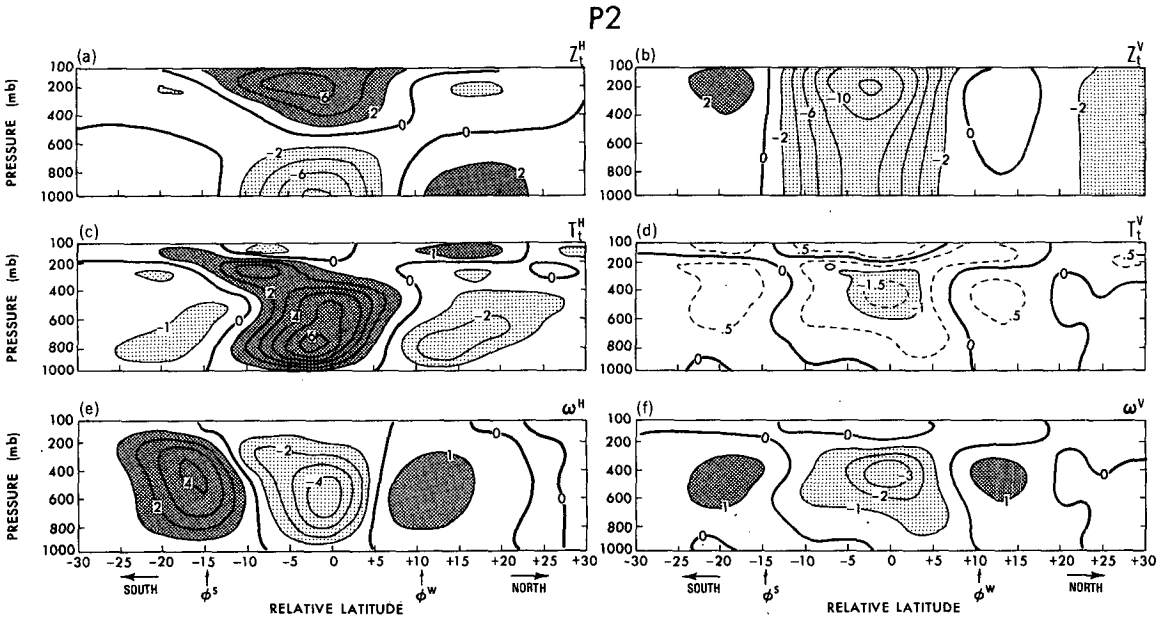

FIG. 8. Meridional cross sections of the regression coefficients of the scaled monthly coefficients of the P2 storm-track mode with eddy-induced height tendency [panels (a) and (b), contour interval: 2×10^{-5} m s^{-1}], temperature tendency [panels (c) and (d), contour interval: 1×10^{-6} °C s^{-1}], and pressure velocity [panels (e) and (f), contour interval: 1×10^{-5} mb s^{-1}]. The effects of the eddy heat fluxes and eddy vorticity fluxes are displayed in the left and right panels, respectively. Results shown here are weighted zonal averages in a coordinate system defined with reference to the bold line in Fig. 2a (see text for details). Positive and negative values along the abscissas indicate poleward and equatorward displacements, respectively, from this bold line. Here ϕ^S and ϕ^W denote the latitudes of anomalously strong and weak synoptic activity, respectively.

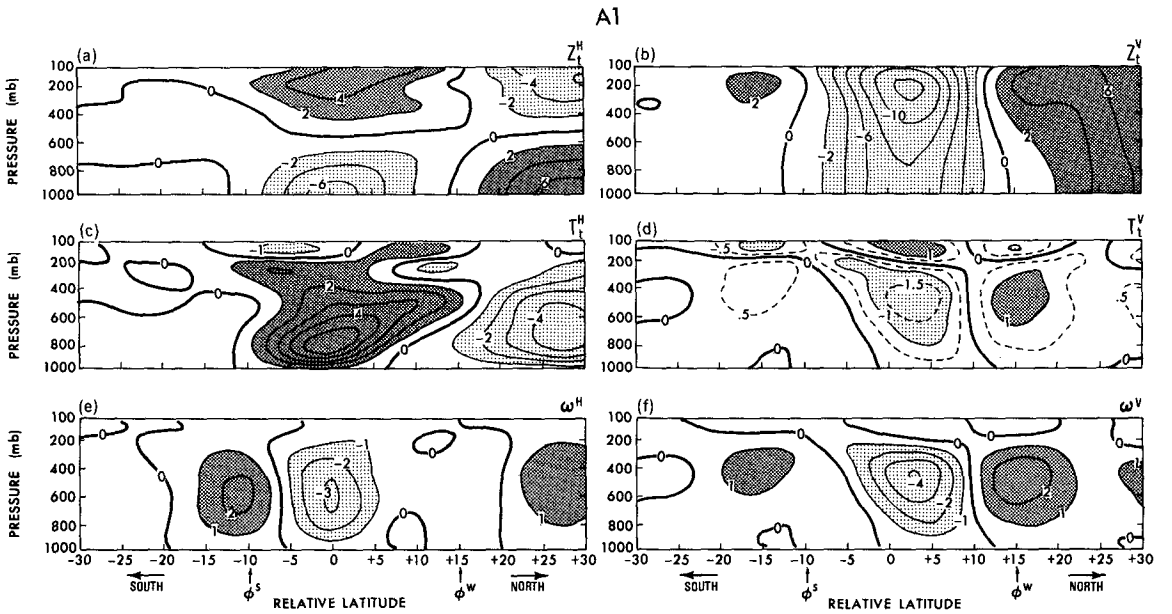

FIG. 9. As in Fig. 8, but for regression coefficients versus time series of the A1 storm-track mode, as obtained by zonal averaging in a coordinate system defined with reference to the bold line in Fig. 3a.

to those noted above at locations with sinking ω^H. Similarly, the results in Figs. 6–9 confirm that rising motion induced by vorticity fluxes is coincident with negative T_t^V, and vice versa.

It is seen from Eq. (3) that eddy vorticity transports lead to vorticity changes (i.e., ζ_t^V) through both the secondary circulation [i.e., the $f(\partial\omega^V/\partial p)$ term] *and* the convergence of eddy vorticity fluxes [the $-(\nabla\cdot\overline{\mathbf{V}'\zeta'})$term]. By the same token, Eq. (4) indicates that θ_t^H result from both the secondary circulation induced by heat transports ($\omega^H S$) *and* eddy flux convergence $-(\nabla\cdot\overline{\mathbf{V}'\theta'})$. It is evident from Fig. 1 and the results shown earlier in this section that ω^H and ω^V act to oppose the effects of the convergence of heat and vorticity fluxes, respectively. For instance, in the region poleward of ϕ^S, the vorticity flux convergence $[-(\nabla\cdot\overline{\mathbf{V}'\zeta'})>0]$ is countered by upper-level divergence of the secondary circulation [i.e., $f(\partial\omega^V/\partial p)<0$, see Figs. 8f and 9f]; and heat flux convergence $[-(\nabla\cdot\overline{\mathbf{V}'\theta'})>0]$ is offset by adiabatic cooling accompanying the ascending branch of the secondary circulation (i.e., $\omega^H S<0$, see Figs. 8e and 9e). Hence, it would be interesting to determine the degree to which the impacts of flux convergences are mitigated by the secondary circulations induced by the same fluxes. We proceed to address this issue by comparing the amplitudes of Z_t^V (and hence, indirectly, ζ_t^V) and T_t^H (shown in Figs. 4–6) with those of the tendencies due to flux convergences alone [i.e., the first term on the rhs of Eqs. (3) and (4)]. The differences noted in such a comparison could then be attributed to the effects of the secondary circulations [i.e., $f(\partial\omega^V/\partial p)$ and $\omega^H S$].

As explained in L (see his section 4b), the convergence of eddy vorticity fluxes yields a height tendency given by $-fg^{-1}\chi^V$, where χ^V is the potential function for the vorticity flux divergence, that is, $\nabla^2\chi^V=\nabla\cdot\overline{\mathbf{V}'\zeta'}$, so that the irrotational component of the eddy vorticity flux vector $(\overline{\mathbf{V}'\zeta'})_\chi$ is given by $\nabla\chi^V$. Analogously, the convergence of eddy heat fluxes yields a temperature tendency given by $-\nabla\cdot\overline{\mathbf{V}'T'}$. The tendencies associated with the vorticity and heat flux divergences have been computed for each winter month in the 81-month data sample by using the bandpass-filtered covariance statistics described in section 2. The regression patterns of the height tendency at 200 mb and temperature tendency at 850 mb thus obtained versus the scaled EOF coefficients for the P2 mode are shown in panels (a) and (c) of Fig. 10. The corresponding patterns for the A1 mode are displayed in Fig. 11. It is seen that a strong spatial resemblance exists between the distributions of $-fg^{-1}\chi^V$ and Z_t^V, and between $-\nabla\cdot\overline{\mathbf{V}'T'}$ and T_t^H. For instance, the region between ϕ^S and ϕ^W is characterized by vorticity flux convergence (i.e., $-fg^{-1}\chi^V<0$, see Figs. 10a and 11a) and negative Z_t^V (Figs. 4c and 5c) at 200 mb, as well as by heat flux convergence $[-(\nabla\cdot\overline{\mathbf{V}'T'})>0$, see Fig. 10c and 11c] and positive T_t^H (Figs. 6a,b) at 850 mb. The amplitudes for Z_t^V and T_t^H are about 70%–80% of the amplitudes for $-fg^{-1}\chi^V$ and $-\nabla\cdot\overline{\mathbf{V}'T'}$. The contributions by the secondary circulations, as deduced from the *differences* between Z_t^V and $-fg^{-1}\chi^V$, and between T_t^H and $-(\nabla\cdot\overline{\mathbf{V}'T'})$, compensate for only 20%–30% of the effects due to flux convergences. Hence, notwithstanding the mitigation by

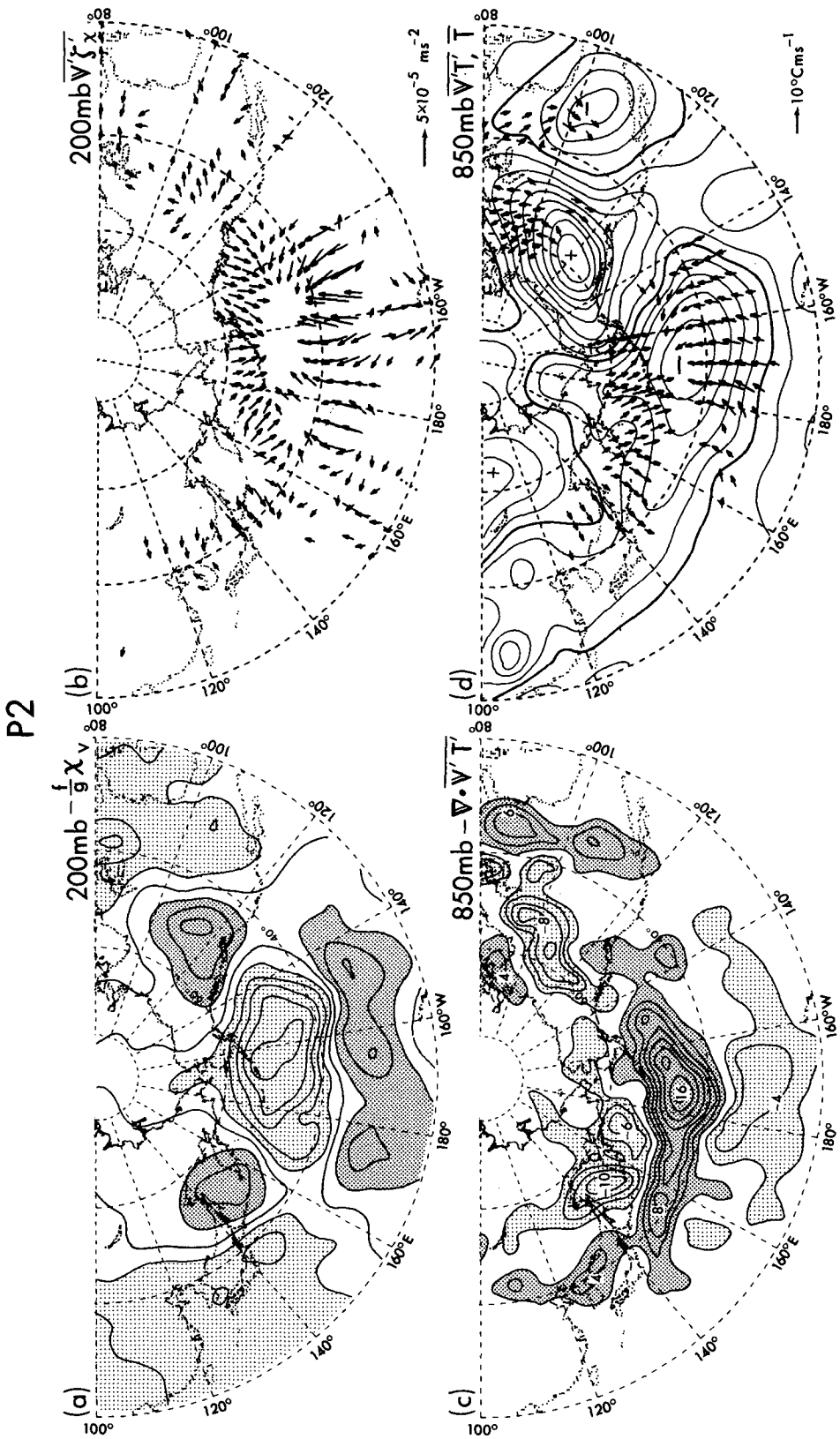

FIG. 10. Distributions of the regression coefficients of the scaled monthly coefficients of the P2 storm-track mode with gridpoint data of (a) $-fg^{-1}\chi^V$ (contour interval: 5×10^{-5} m s^{-1}) and (b) $(\overline{V'\zeta'})_\chi$ (scale for vectors given at the lower right) at 200 mb, and with (c) $-(\nabla\cdot\overline{V'T'})$ (contour interval: 2×10^{-6} °C s^{-1}) and (d) $\overline{V'T'}$ (vectors, scale given at the lower right) and monthly mean temperature anomaly (contours, interval: 1°C) at 850 mb. See text for definitions of symbols.

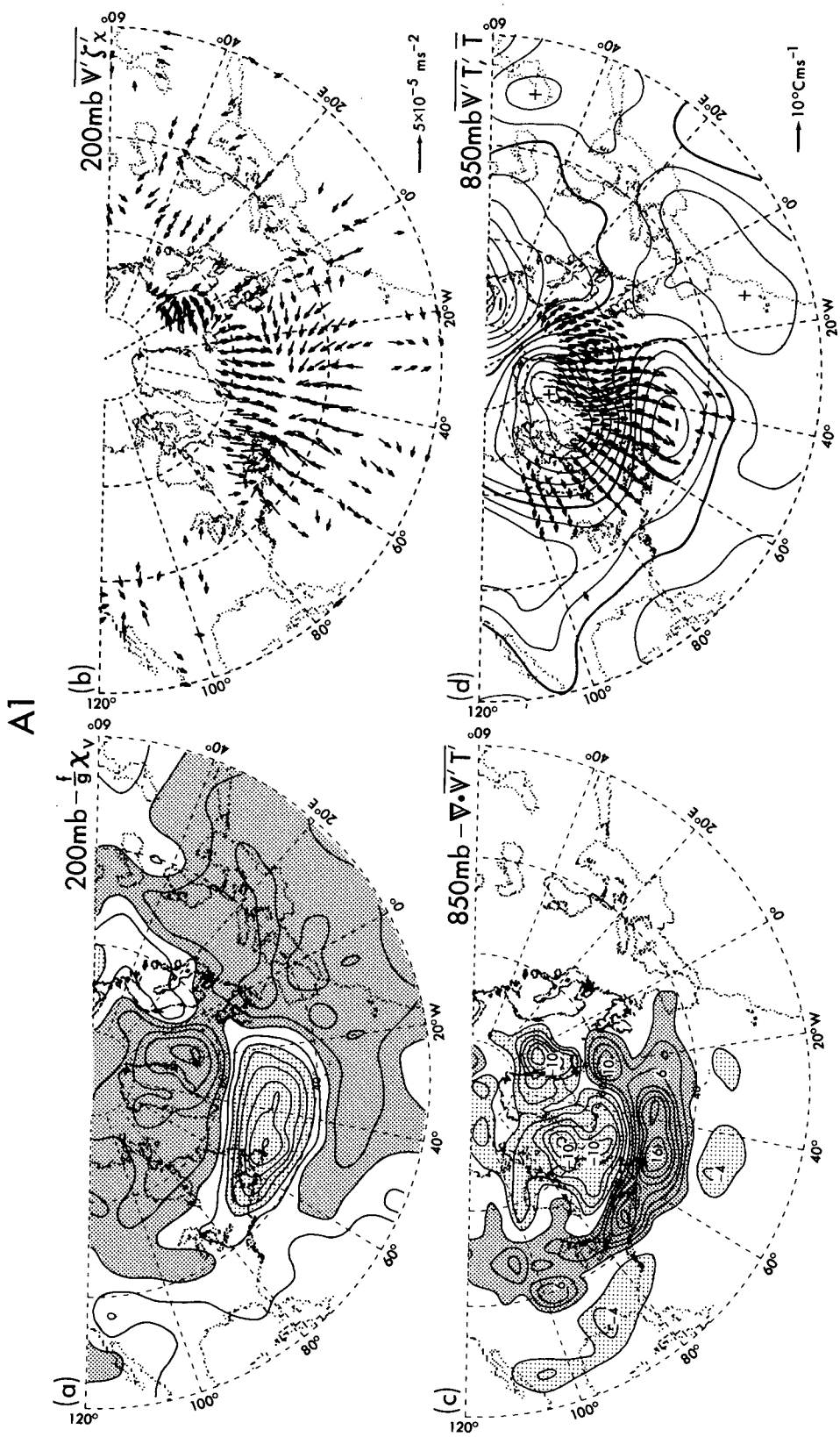

FIG. 11. As in Fig. 10, but for regression coefficients versus time series of the A1 storm-track mode.

the secondary circulations, the essential characteristics of the net tendencies Z_t^V and T_t^H are primarily determined by the convergence patterns of eddy vorticity and heat fluxes, respectively. Lau and Holopainen (1984) have come to a similar conclusion by examining T_t^H and $-\nabla \cdot \overline{\mathbf{V}'T'}$ averaged over an eight-winter period. The diagnosis of zonally averaged budgets by Pfeffer (1981) also indicates that the effects of eddy flux convergences are stronger than the opposing effects of the secondary circulations.

To gain an appreciation of the heat and vorticity transports responsible for the flux convergence patterns in the left panels of Figs. 10 and 11, the regression values of the P2 and A1 coefficients versus the zonal and meridional components of the eddy transports are displayed in panels (b) and (d) of the same figures in a vectorial format. Since the vorticity flux vector field contains a substantial nondivergent component (see Lau and Wallace 1979), which does not contribute to vorticity and height tendencies, we have chosen to show only the irrotational component of this flux vector, that is, $(\overline{\mathbf{V}'\zeta'})_\chi$, in panels (b). The heat flux vector field in the lower troposphere is dominated by the irrotational component, hence the regression patterns for the total flux vector $\overline{\mathbf{V}'T'}$ are presented in panels (d). Superimposed on the latter panels are the corresponding regression contours for the monthly averaged 850-mb temperature anomaly (see Figs. 2f and 3f), so as to illustrate local relationships between the heat flux vectors and the concurrent monthly mean temperature changes.

Inspection of the right panels of Figs. 10 and 11 indicates that anomalous poleward heat and vorticity fluxes prevail over the latitude of enhanced eddy amplitudes ϕ^S, whereas the regions along ϕ^W are characterized by anomalous equatorward heat and vorticity fluxes. The behavior of these transport properties in relation to the sites of eddy activity is consistent with the discussion on the nature of the eddy forcing in section 3 (see also Fig. 1). Within the region between ϕ^S and ϕ^W, the anomalous fluxes associated with P2 and A1 lead to strong convergences of eddy heat and vorticity transports, which is consistent with the features in the left panels of Figs. 10 and 11. Comparison between the regression patterns for $(\overline{\mathbf{V}'\zeta'})_\chi$ and the corresponding charts for the monthly mean 1000-mb height (Figs. 2d and 3d) reveals that the air columns above the anomalous monthly mean low pressure centers are characterized by vorticity flux convergence, and vice versa. This relationship between the upper-level vorticity transport and lower-level mean pressure field has been noted by Lau and Wallace (1979) in a climatological context, and is suggestive of the important role of the frictional drag accompanying the near-surface flow in counterbalancing the vorticity flux divergence directly aloft. The regression charts for $\overline{\mathbf{V}'T'}$ (Figs. 10d and 11d) exhibit a well-defined relationship with the monthly mean temperature anomaly fields (see contours on the same figures), with the heat flux vectors being directed down the anomalous local temperature gradient. Hence, the divergence of the eddy heat transports in individual months acts to dissipate the temperature anomalies for the same month. An analogous result has been reported by Lau and Wallace (1979) on the basis of long-term averaged statistics, and by Edmon (1980) on the basis of two specific winters.

Following Andrews and McIntyre (1976), the net effects of eddy flux convergences and eddy-induced secondary circulations may be represented by a "residual circulation" defined as

$$\tilde{\omega} = \omega^H + \omega^V - \left(\frac{\nabla \cdot \overline{\mathbf{V}'\theta'}}{S}\right),$$

so that Eqs. (3) and (4) may be rewritten as [see Hoskins 1983, Eqs. (7.40) and (7.43′)]

$$\begin{aligned} \zeta_t^{H+V} &= -(\nabla \cdot \overline{\mathbf{V}'\zeta'}) + f\frac{\partial}{\partial p}\left(\frac{\nabla \cdot \overline{\mathbf{V}'\theta'}}{S}\right) + f\frac{\partial}{\partial p}\tilde{\omega} \\ &= -(\nabla \cdot \overline{\mathbf{V}'q'}) + f\frac{\partial}{\partial p}\tilde{\omega}, \end{aligned} \tag{5}$$

and

$$\theta_t^{H+V} = \tilde{\omega}S, \tag{6}$$

where q is the quasigeostrophic potential vorticity. Hence, the eddy-induced temperature tendency is solely determined by adiabatic processes associated with the residual circulation [Eq. (6)], and the vorticity tendency is given as the sum of the flux convergence of q and the stretching effects accompanying the residual circulation [Eq. (5)].

We shall not perform a detailed diagnosis of the eddy forcing within the framework of Eqs. (5) and (6). However, a few remarks will be made concerning the qualitative nature of the residual circulation $\tilde{\omega}$ on the basis of the results presented in this section. Recalling that $\theta_t^H \gg \theta_t^V$ (Fig. 6), and $\theta_t^H \approx -(\nabla \cdot \overline{\mathbf{V}'\theta'})$ (Figs. 6, 10, and 11), it follows from Eq. (4) that $\theta_t^{H+V} \approx -(\nabla \cdot \overline{\mathbf{V}'\theta'})$. The relationship in Eq. (6) then requires that the anomalous residual circulation be characterized by subsidence (i.e., $\tilde{\omega} > 0$) poleward of ϕ^S [where $-(\nabla \cdot \overline{\mathbf{V}'\theta'} > 0$] and ascent equatorward of ϕ^S. The relative contributions of the stretching effects of this residual circulation $[f(\partial\tilde{\omega}/\partial p)]$ and the convergence of potential vorticity fluxes $-(\nabla \cdot \overline{\mathbf{V}'q'})$ to the net vorticity tendency in Eq. (5) remain to be ascertained by actual evaluations of these two terms separately.

6. Generalized relationships between the eddy forcing and the local monthly averaged anomaly

The results presented in the previous section are based on regression charts of various eddy forcing terms versus the time series of two particular modes of storm-track variability, that is, P2 and A1. In this section, we proceed to demonstrate that the principal findings re-

ported in section 5 are not just restricted to the specific storm-track changes associated with the P2 and A1 modes, but have much wider applications to local interactions between synoptic-scale processes and the low-frequency circulation changes. In order to appreciate the generality of the results reported earlier in this study, we shall no longer use the time series of any storm-track mode as the basis for the following computations. Instead, we shall examine the local relationships between the eddy forcing and the concurrent monthly mean anomaly for every month in the 81-month dataset, without regard to the prevalent mode of storm-track variability in individual months. These relationships will be illustrated by calculating the regression coefficients of the time series of eddy-induced height or temperature *tendencies* at individual grid points versus the time series of monthly averaged height or temperature *anomalies* at the same grid points. In this regression analysis, the tendencies are treated as the dependent variable, and the anomalies are treated as the independent variable. The effects of various eddy forcings on the local monthly mean circulation may be assessed by mapping the regression coefficients thus obtained. The reciprocal of these coefficients also provides for a convenient measure of the characteristic time scales of the eddy processes in question.

Figure 12 shows the distributions of the regression coefficients of Z_t^H [panels (a) and (b)] and Z_t^V [panels (c) and (d)] versus the local monthly mean height anomaly at the corresponding pressure levels. Results for the 200- and 1000-mb levels are presented on the right and left halves of the figure, respectively. The statistical significance of the regression coefficients at individual grid points has been tested using the procedure described by Nakamura et al. (1987). These computations (not shown) indicate that the principal features in Fig. 12 exceed the 95% confidence level. The polarity of the values displayed in Fig. 12 indicates whether the eddy tendency is reinforcing (positive coefficients) or dissipating (negative coefficients) the local monthly mean anomaly.

The patterns associated with eddy heat fluxes (Figs. 12a,b) are dominated by zonally elongated extrema over the North Pacific and eastern North America–North Atlantic regions. These features are almost collocated with the climatological axes of the two principal wintertime storm tracks (e.g., see Fig. 1 of L). It is seen that the baroclinic eddy processes in these active sites act to destroy the local monthly mean height anomalies at 200 mb, whereas the same processes tend to reinforce the local height anomalies at 1000 mb. The typical time scales associated with these processes, as estimated from the reciprocal of the values displayed in Figs. 12a,b, range from 1–2 months at 200 mb to 15–30 days at 1000 mb.

The effects of eddy vorticity transports on the local monthly mean heights are also strongest over the northern oceans (Figs. 12c,d). The vorticity fluxes tend to reinforce the local height changes at both the upper and lower levels. The regression values in Fig. 12d are somewhat larger than those in Fig. 12c, thus suggesting that the eddy barotropic forcing is more effective at 1000 mb than at 200 mb. The corresponding time scales for eddy vorticity forcing are approximately 20–30 days at 200 mb, and 15–20 days at 1000 mb.

Comparison among the four panels of Fig. 12 reveals that the local relationship between Z_t^H and the height anomaly is most evident over the two storm-track regions, and it considerably weakens farther downstream, whereas the relationship between Z_t^V and the height anomaly is sustained downstream of the storm tracks. At the 200-mb level, the regression coefficients associated with the eddy barotropic forcing are larger than those for the (opposing) baroclinic forcing. On the other hand, the eddy heat fluxes are more effective than the vorticity fluxes in inducing height changes at 1000 mb.

Due to the cancellations at 200 mb between the forcings associated with heat and vorticity fluxes, the regression coefficients for the total eddy-induced tendency Z_t^{H+V} at that level (not shown) are smaller than the corresponding values obtained by examining Z_t^H and Z_t^V separately (Figs. 12a and 12c). The time scale for Z_t^{H+V} at 200 mb is approximately 30–40 days and is considerably longer than the time scale (7–10 days) estimated in L by visual inspection of composite charts for vorticity forcing only. As a result of the cooperation of the heat and vorticity transports to reinforce the monthly mean height changes at 1000 mb, the time scale for the combined forcing at that level is as short as several days along the axes of the climatological storm tracks. Hence, the total eddy forcing of the monthly mean heights due to baroclinic and barotropic processes is much more efficient at 1000 mb than at 200 mb.

In Fig. 13 the 850-mb distribution of the regression coefficient of T_t^H versus the monthly mean temperature is shown. The extrema in this figure also surpass the 95% significance level. The prominent features in Fig. 13 are located in the two storm-track regions. A third extremum occurs in the European sector. The prevalent negative values in this chart are indicative of the role of eddy heat transports to dissipate the local monthly mean temperature anomalies. The typical time scale for this process is approximately 10–15 days in the storm-track regions.

In summary, the present results derived from local regression between transient eddy forcing and monthly mean anomalies serve to generalize the findings in section 5 on the behavior of eddy processes in relation to the P2 and A1 storm-track modes. The evidence presented here confirms the vertical dependence of the effects of eddy heat and vorticity fluxes on the local monthly mean height anomaly. The inferences in this section on the relative importance of the eddy forcings due to heat and vorticity transports at various altitudes

are also consistent with those drawn in the previous section.

7. Discussion

The relationships between the *climatological* mean synoptic-scale eddy forcing and the *long-term averaged* circulation have been examined in some detail by LH. The results from the present analysis illustrate that these relationships still hold for variations in the eddy forcing and the ambient circulation *on a month-to-month basis*. These new findings also complement the previous work by L, who only considered the effects of eddy

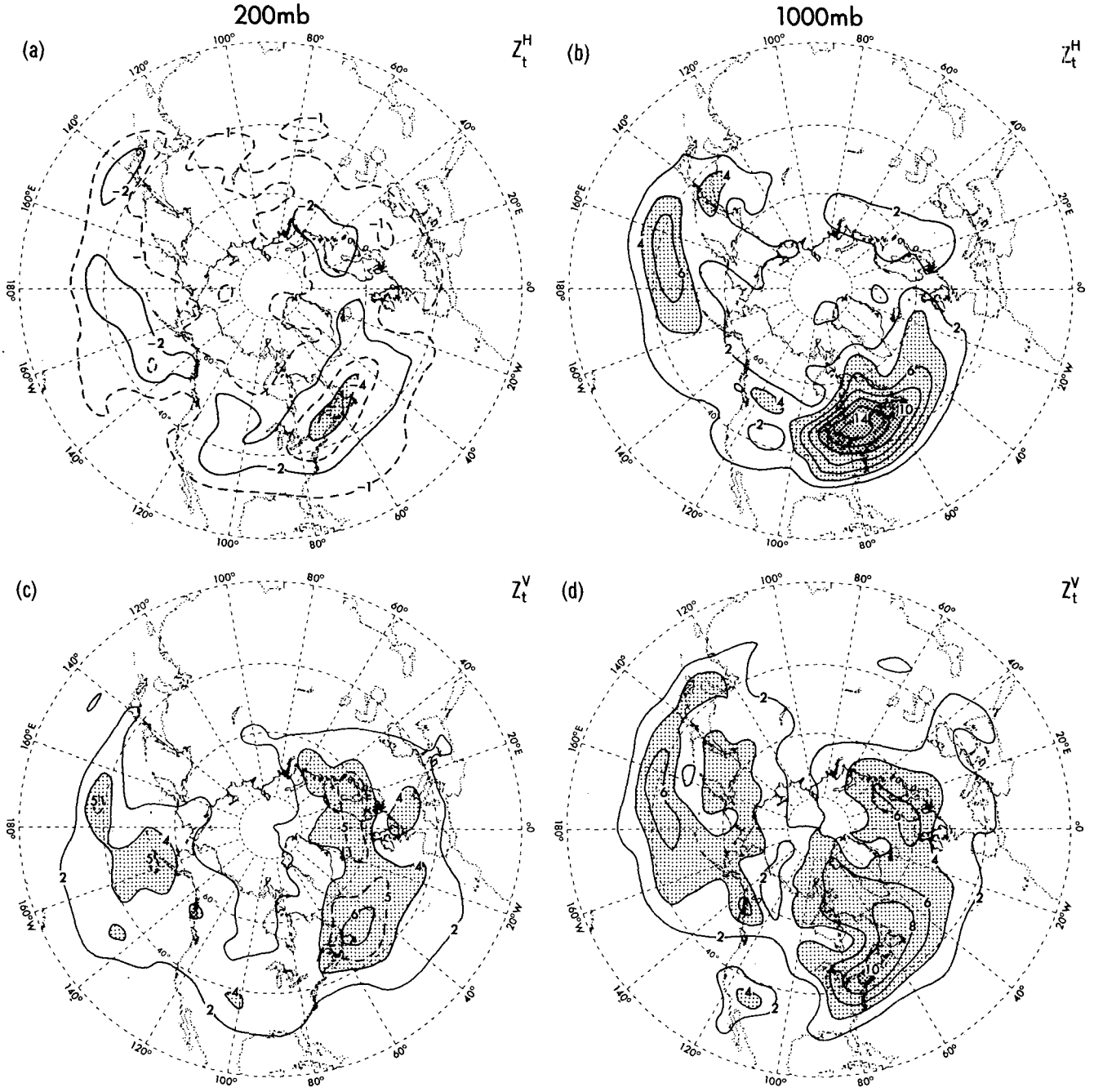

FIG. 12. Distributions of the regression coefficients of gridpoint data of monthly averaged height anomaly with the local height tendency induced by eddy heat fluxes [panels (a) and (b)] and eddy vorticity fluxes [panels (c) and (d)]. Results for the 200- and 1000-mb levels are displayed in the left and right panels, respectively. Interval between solid contours: 0.02 day^{-1}. Light and dense stippling indicate values larger than 0.04 and 0.1 day^{-1}, respectively. The zero contour is omitted.

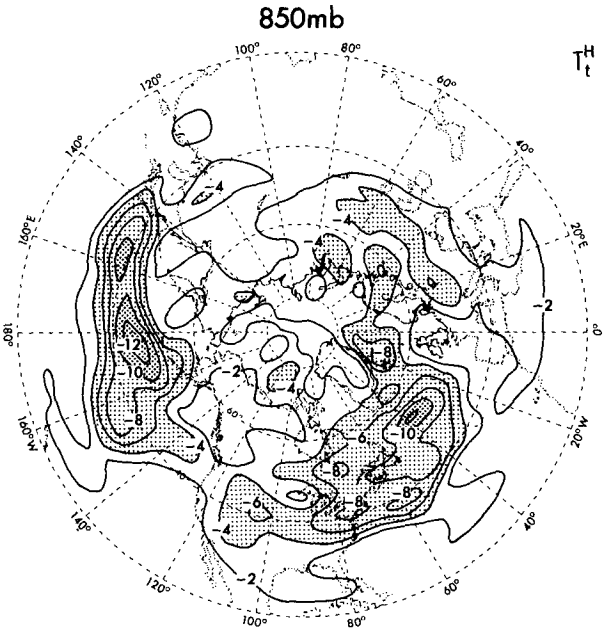

FIG. 13. Distribution of the regression coefficients of gridpoint data of monthly averaged temperature anomaly at 850 mb with the local temperature tendency induced by eddy heat fluxes. Interval between solid contours: 0.02 day^{-1}. Light and dense stippling indicate values larger than 0.04 and 0.1 day^{-1}, respectively. The zero contour is omitted.

vorticity fluxes on the monthly mean flow at the 300-mb level. By including the eddy forcing due to heat fluxes, and by extending the diagnosis to the entire atmospheric column from 1000 to 100 mb, we have come to the conclusion that, whereas Z_t^H does oppose Z_t^V in the upper troposphere, the magnitude of the latter effect is larger, so that the effect of the residue Z_t^{H+V} on the monthly mean circulation is still similar to, but weaker than, that of Z_t^V. Hence, the qualitative aspect of the conclusion drawn in L—that the synoptic-scale eddies act to reinforce the slowly varying component of the flow field in the upper troposphere—is still valid even after the baroclinic effects are taken into account. However, as a result of the partial cancellation between Z_t^H and Z_t^V, this reinforcement is now seen to be less effective than was noted previously.

The observed tendency for the synoptic-scale baroclinic processes to dissipate the monthly mean height anomalies in the upper troposphere, and for the barotropic processes to reinforce the same anomalies, are in accord with numerical studies of the life cycles of unstable baroclinic waves, such as those performed by Simmons and Hoskins (1978). These model experiments indicate that the growth phase of such disturbances is accompanied by vigorous poleward heat transports, which act to reduce the meridional temperature gradient and the thermal wind of the mean flow. This baroclinic stage is typically followed by an occlusion phase, during which barotropic processes dominate, with momentum fluxes acting to accelerate the mean flow at the upper levels. The extension of large regression values for Z_t^V toward the downstream (eastern) portion of the North Atlantic storm track (Fig. 12c), where the disturbances frequently occlude, appears to attest to the above model scenario. The gross properties of the eddy forcing as deduced using height tendencies here are also in accord with the findings on eddy–mean flow interaction reported by Hoskins et al. (1983, see the schematic diagram in their Fig. 13) using Eliassen–Palm flux vectors. By using the same quasi-geostrophic framework as that described in section 3, Mullen (1987) has performed a comprehensive composite study of the transient eddy forcing during specific blocking episodes identified in the observed and model-simulated atmospheres. The vertical structure of the height tendencies induced separately by the synoptic-scale eddy heat and vorticity fluxes, as deduced in Mullen's case study approach, are in qualitative agreement with the results of the present statistical study, which incorporates the information for every winter month in the 81-month dataset. Similar to our study, Mullen noted the out-of-phase relationship between T_t^H and the mean lower-tropospheric temperature anomaly of the blocking ridge. However, his analysis also suggests that the maximum in Z_t^V is shifted upstream of the blocking ridge by almost a quarter wavelength. On the other hand, our results indicate that, for the 81 monthly samples as a whole, the pattern of Z_t^V exhibits a relatively smaller spatial displacement from the monthly mean height anomaly (compare Fig. 4c with Fig. 2c, and Fig. 5c with Fig. 3c). The three-dimensional structure of the eddy-induced height tendency (Figs. 4–5) bears a considerable resemblance to that associated with the most unstable local mode for a zonally inhomogeneous baroclinic basic flow, as reported in the modeling study by Cai and Mak (1990, see their Fig. 9).

As a result of the partial cancellation between Z_t^H and Z_t^V in the upper troposphere, and the reinforcement between Z_t^H and Z_t^V near the lower boundary, the net height tendency induced by synoptic-scale eddies is strongest at the 1000-mb level, and gradually weakens with increasing altitude. In view of the relatively weak eddy forcing near the tropopause level, other mechanisms, such as orographic effects, heating, and influences of lower-frequency fluctuations, probably need to be taken into account in understanding the variability of the circulation patterns in the upper troposphere on monthly and seasonal time scales. On the other hand, the much stronger forcing of the near-surface wind circulation by synoptic-scale eddies could exert a considerable influence on the thermal and dynamical behavior of the underlying ocean. Experiments with general circulation models have demonstrated a marked sensitivity of the strength and location of the storm tracks to the presence of extratropical sea surface temperature anomalies (Palmer and Sun 1985; Lau

and Nath 1990). The eddy-induced tendencies at the air–sea interface could well turn out to be an important factor in advancing our knowledge of the feedback processes at the atmosphere–ocean interface in the middle latitudes.

Our study is exclusively concerned with the forcing due to transient disturbances with time scales of several days. To gain some appreciation of the forcing due to eddies with relatively longer time scales, it is useful to recall some of the results presented by LH on the basis of climatologically averaged statistics. This previous study has noted that the three-dimensional structure of, and the relationships between, Z_t^H and Z_t^V due to transient eddies with time scales ranging from 10 days to a season (referred to as the "low-pass" fluctuations in LH) are radically different from the corresponding results for synoptic-scale eddies, as reported in the present paper. In particular, it was shown in LH that Z_t^H and Z_t^V associated with low-pass eddies actually reinforce each other in the upper troposphere, whereas some cancellation between the two tendency terms occurs at the lower levels (see Fig. 5 of LH). Moreover, both Z_t^H and Z_t^V for the low-pass fluctuations act to dissipate the long-term averaged stationary wave at 300 mb. Hence, it is worth expanding the scope of the present work by applying the tools developed here to evaluate the impact of such low-pass phenomena with characteristic time scales beyond several days.

It needs to be emphasized that the present study is primarily concerned with the representation of the effects of eddy flux divergences in terms of geostrophically and hydrostatically balanced *tendencies*. Whereas these tendencies are helpful in the understanding of the three-dimensional nature of the transient eddy forcing in relation to the sites of synoptic activity and the background flow structure, such tendencies do not in themselves furnish information on the *steady-state response* to the eddy transports. The latter response must ultimately be obtained as solutions to stationary-wave numerical models in which the eddy forcing is balanced by mean flow advection as well as various diabatic processes such as heating and friction. The impact of transient eddy fluxes and other forcing terms on these stationary solutions has been examined by Youngblut and Sasamori (1980), Valdes and Hoskins (1989), and Hoskins and Valdes (1990), among others. We envision that the tendency method outlined in section 3 could serve as a useful diagnostic tool for shedding light on the nature of the stationary model responses to various forcing mechanisms other than eddy effects. For instance, one could conceivably extend the scope of the present study by replacing the eddy forcing terms on the rhs of Eqs. (1) and (2) with terms corresponding to other relevant processes, such as linear or nonlinear heat and vorticity advection by the monthly mean flow, latent and sensible heating, orographic influences, and frictional dissipation, and then solve for the height tendency and vertical motion associated with these individual processes separately. Intercomparison among these results would yield considerable insight on the roles of different forcing components in maintaining the stationary atmospheric response. These additional complications notwithstanding, the remarkable spatial correspondence between the patterns of Z_t^{H+V} and the monthly mean height anomaly at 1000 mb (compare Fig. 4f with Fig. 2d, and Fig. 5f with Fig. 3d) suggest that the phase of the stationary response can be almost the same as that of the eddy-induced tendency under certain circumstances. In this particular instance, the effect of Z_t^{H+V} at 1000 mb is most likely being balanced locally by friction, whereas mean flow advection near the lower boundary (which would lead to a quadrature relationship between the steady-state response and the eddy forcing) apparently plays a secondary role.

The modeling studies of Valdes and Hoskins (1989) and Hoskins and Valdes (1990) indicate that the vertical component of the eddy heat transports, as well as the latent and sensible heating accompanying the passage of transient disturbances, play substantial roles in forcing the stationary flow field. The importance of latent heat release in the development of a synoptic system has also been noted in the case study by Pauley and Smith (1988) using an extended version of the height tendency equation, which explicitly incorporates the effects of diabatic heating, and allows for variations of the static stability parameter in all three dimensions (see Tsou et al. 1987). Owing to the lack of reliable observations of the vertical wind velocity and diabatic heating rates, these additional eddy effects cannot be assessed in the present study. With the advent of realistic simulations of the stationary waves and the storm tracks by high-resolution general circulation models, perhaps the diagnosis of such model output will provide a more comprehensive understanding of the total transient eddy effect than is attempted here.

Acknowledgments. I. M. Held and S. T. Garner have examined an initial draft of this paper; their insightful comments have helped us to clarify the roles of eddy flux convergences and secondary circulations. E. O. Holopainen, J. R. Lanzante, and H. Nakamura have also read this manuscript and offered useful suggestions. The official reviewers have made constructive comments, many of which were incorporated in the revised version of this paper. The NMC analyses used in this study were assembled at the University of Washington. E. E. Recker and J. M. Wallace have kindly made this dataset available to us. The GFDL Scientific Illustration Group at GFDL prepared the figures.

REFERENCES

Anderson, J. R., and J. R. Gyakum, 1989: A diagnostic study of Pacific basin circulation regimes as determined from extratropical cyclone tracks. *Mon. Wea. Rev.*, **117**, 2672–2686.

Andrews, D. G., and M. E. McIntyre, 1976: Planetary waves in hor-

izontal and vertical shear: The generalized Eliassen–Palm relation and the mean zonal acceleration. *J. Atmos. Sci.*, **33**, 2031–2048.

Blackmon, M. L., 1976: A climatological spectral study of the 500 mb geopotential height of the Northern Hemisphere. *J. Atmos. Sci.*, **33**, 1607–1623.

——, and N.-C. Lau, 1980: Regional characteristics of the Northern Hemisphere wintertime circulation: A comparison of the simulation of a GFDL general circulation model with observations. *J. Atmos. Sci.*, **37**, 497–514.

——, J. M. Wallace, N.-C. Lau, and S. L. Mullen, 1977: An observational study of the Northern Hemisphere wintertime circulation. *J. Atmos. Sci.*, **34**, 1040–1053.

Bretherton, F. B., 1966: Critical layer instability in baroclinic flows. *Quart. J. Roy. Meteor. Soc.*, **92**, 325–334.

Cai, M., and M. Mak, 1990: On the basic dynamics of regional cyclogenesis. *J. Atmos. Sci.*, **47**, 1417–1442.

Dole, R. M., 1989: Life cycles of persistent anomalies. *Mon. Wea. Rev.*, **117**, 177–211.

Edmon, H. J., Jr., 1980: A study of the general circulation over the Northern Hemisphere during the winters of 1976/77 and 1977/78. *Mon. Wea. Rev.*, **108**, 1538–1553.

Holopainen, E. O., 1978: On the dynamic forcing of the long-term mean flow by the large-scale Reynolds' stresses in the atmosphere. *J. Atmos. Sci.*, **35**, 1596–1604.

——, 1990: Role of cyclone-scale eddies in the general circulation of the atmosphere: A review of recent observational studies. *Extratropical Cyclones: The Erik Palmen Memorial Volume*, C. W. Newton and E. O. Holopainen, Eds., Amer. Meteor. Soc., 48–62.

——, and C. Fortelius, 1987: High-frequency transient eddies and blocking. *J. Atmos. Sci.*, **44**, 1632–1645.

Holton, J. R., 1979: *An Introduction to Dynamic Meteorology*. 2d ed. Academic Press, 391 pp.

Hoskins, B. J., 1983: Modelling of the transient eddies and their feedback on the mean flow. *Large-Scale Dynamical Processes in the Atmosphere*, B. J. Hoskins and R. P. Pearce, Eds., Academic Press, 397 pp.

——, and P. J. Valdes, 1990: On the existence of storm-tracks. *J. Atmos. Sci.*, **47**, 1854–1864.

——, I. N. James, and G. H. White, 1983: The shape, propagation, and mean-flow interaction of large-scale weather systems. *J. Atmos. Sci.*, **40**, 1595–1612.

Lau, N.-C., 1979: The observed structure of tropospheric stationary waves and the local balances of vorticity and heat. *J. Atmos. Sci.*, **36**, 996–1016.

——, 1988: Variability of the observed midlatitude storm tracks in relation to low-frequency changes in the circulation pattern. *J. Atmos. Sci.*, **45**, 2718–2743.

——, and E. O. Holopainen, 1984: Transient eddy forcing of the time-mean flow as identified by geopotential tendencies. *J. Atmos. Sci.*, **41**, 313–328.

——, and M. J. Nath, 1990: A general circulation model study of the atmospheric response to extratropical SST anomalies observed in 1950–79. *J. Climate*, **3**, 965–989.

——, and J. M. Wallace, 1979: On the distribution of horizontal transports by transient eddies in the Northern Hemisphere wintertime circulation. *J. Atmos. Sci.*, **36**, 1844–1861.

Metz, W., 1989: Low-frequency anomalies of atmospheric flow and the effects of cyclone-scale eddies: A canonical correlation analysis. *J. Atmos. Sci.*, **46**, 1026–1041.

Mullen, S. L., 1987: Transient eddy forcing of blocking flows. *J. Atmos. Sci.*, **44**, 3–22.

Nakamura, H., and J. M. Wallace, 1990: Observed changes in baroclinic wave activity during the life cycles of low-frequency circulation anomalies. *J. Atmos. Sci.*, **47**, 1100–1116.

——, M. Tanaka, and J. M. Wallace, 1987: Horizontal structure and energetics of Northern Hemisphere wintertime teleconnection patterns. *J. Atmos. Sci.*, **44**, 3377–3391.

Palmer, T. N., and Z.-B. Sun, 1985: A modelling and observational study of the relationship between sea surface temperature in the northwest Atlantic and the atmospheric general circulation. *Quart. J. Roy. Meteor. Soc.*, **111**, 947–975.

Pauley, P. M., and P. J. Smith, 1988: Direct and indirect effects of latent heat release on a synoptic-scale wave system. *Mon. Wea. Rev.*, **116**, 1209–1235.

Pfeffer, R. L., 1981: Wave–mean flow interactions in the atmosphere. *J. Atmos. Sci.*, **38**, 1340–1359.

Plumb, R. A., 1986: Three-dimensional propagation of transient quasigeostrophic eddies and its relationship with the eddy forcing of the time-mean flow. *J. Atmos. Sci.*, **43**, 1657–1670.

Rogers, J. C., 1990: Patterns of low frequency monthly sea level pressure variability (1899–1986) and associated wave cyclone frequencies. *J. Climate*, **3**, 1899–1986.

Simmons, A. J., and B. J. Hoskins, 1978: The life cycles of some nonlinear baroclinic waves. *J. Atmos. Sci.*, **35**, 414–432.

Trenberth, K. E., 1986: An assessment of the impact of transient eddies on the zonal flow during a blocking episode using localized Eliassen–Palm flux diagnostics. *J. Atmos. Sci.*, **43**, 2070–2087.

Tsou, C.-H., P. J. Smith, and P. M. Pauley, 1987: A comparison of adiabatic and diabatic forcing in an intense extratropical cyclone system. *Mon. Wea. Rev.*, **115**, 763–786.

van Loon, H., and J. C. Rogers, 1978: The seesaw in winter temperatures between Greenland and Northern Europe. Part I: General description. *Mon. Wea. Rev.*, **106**, 296–310.

Valdes, P. J., and B. J. Hoskins, 1989: Linear stationary wave simulations of the time-mean climatological flow. *J. Atmos. Sci.*, **46**, 2509–2527.

Wallace, J. M., and D. S. Gutzler, 1981: Teleconnections in the geopotential height field during the Northern Hemisphere winter. *Mon. Wea. Rev.*, **109**, 784–812.

——, and N.-C. Lau, 1985: On the role of barotropic energy conversion in the general circulation. *Adv. Geophys.*, **28A**, 33–74.

Youngblut, C., and T. Sasamori, 1980: The nonlinear effects of transient and stationary eddies on the winter mean circulation. Part I: Diagnostic analysis. *J. Atmos. Sci.*, **37**, 1944–1957.